



**HAL**  
open science

# Generating Realistic Facial Expressions with Wrinkles for Model-Based Coding

Lijun Yin, Anup Basu

► **To cite this version:**

Lijun Yin, Anup Basu. Generating Realistic Facial Expressions with Wrinkles for Model-Based Coding. Computer Vision and Image Understanding, 2001, 84 (2), pp.201-240. 10.1006/cviu.2001.0949 . hal-03224826

**HAL Id: hal-03224826**

**<https://hal.science/hal-03224826>**

Submitted on 12 May 2021

**HAL** is a multi-disciplinary open access archive for the deposit and dissemination of scientific research documents, whether they are published or not. The documents may come from teaching and research institutions in France or abroad, or from public or private research centers.

L'archive ouverte pluridisciplinaire **HAL**, est destinée au dépôt et à la diffusion de documents scientifiques de niveau recherche, publiés ou non, émanant des établissements d'enseignement et de recherche français ou étrangers, des laboratoires publics ou privés.

# Generating Realistic Facial Expressions with Wrinkles for Model-Based Coding

Lijun Yin

*Department of Computer Science, Thomas J. Watson School of Engineering and Applied Science,  
SUNY Binghamton, Binghamton, New York 13902*

and

Anup Basu<sup>1</sup>

*Department of Computing Science, University of Alberta, Edmonton, Alberta, T6G 2H1, Canada*

Received October 25, 1999; accepted November 20, 2001

---

Due to the limitations of current computer graphics technology mimicking realistic facial textures, such as wrinkles, is very difficult. Facial texture updating and compression are crucial to achieving realistic facial animation for low bit rate model-based coding. In this paper, we present a partial texture updating method for realistic facial expression synthesis with facial wrinkles. First, fiducial points on a face are estimated using a color-based deformable template matching method. Second, an extended dynamic mesh matching algorithm is developed for face tracking. Next, textures of interest (TOI) in the potential expressive wrinkles and mouth–eye texture areas are captured by the detected fiducial points. Among the TOI, the so-called active textures or expressive textures are extracted by exploring temporal correlation information. Finally, the entire facial texture is synthesized using the active texture. Compared to the entire texture updating scheme, partially updating and compressing facial textures significantly reduce the computational complexity and bit rates while still producing an acceptable visual quality. Experiments on the video sequences demonstrate the advantage of the proposed algorithm. © 2001 Elsevier Science (USA)

*Key Words:* texture coding; MPEG4; model-based coding; feature detection; SNHC.

---

<sup>1</sup> This work is supported in part by the Canadian Natural Sciences and Engineering Research Council and Rice Scholarship in Communications. Corresponding author: [anup@cs.ualberta.ca](mailto:anup@cs.ualberta.ca).

## 1. INTRODUCTION

Keeping high fidelity and reducing the number of bits transmitted are the major objectives in realizing low bit rate video coding. Recently, research on synthetic/natural hybrid coding (SNHC) [1, 3, 15], formed within MPEG-4 [22, 32, 33, 41], has been intensified in the aspects of scalable texture coding, animation and model-based coding on body and face models, image analysis and synthesis, object modeling, and 3D model compression. Model-based coding in the scenario of a talking face is a typical application of SNHC. Until now, most work in the field of model-based coding has concentrated on facial feature detection, 3D facial model adaptation, and motion estimation and tracking [2, 6, 35]; little investigation has been done into strategies for facial texture updating and encoding. Accuracy in 3D geometry and face texture contribute to the reconstruction of realistic facial expressions. The vivid facial textures, such as furrows, which are generated by different expressions, are very difficult to capture and model. To create these features using geometric data (geometric model) rather than texture data would require an extremely detailed 3D capture of the face geometry, and a resulting high polygon count in the 3D model. In addition, shading these details properly, if they were represented geometrically, would be very difficult since it would require computing shadows and possibly even diffuse inter-reflection effects to look realistic. The most widely used facial action coding system [10], the representation of facial motion, has also been shown to have difficulty producing a large variety of complicated facial expressions [16]. Due to these difficulties in current computer graphics technology, facial texture extraction and update are the best choices for our current application. If facial texture can be updated for every frame, the subtle change of facial textures (e.g., facial wrinkles) generated by a variety of expressions can be easily captured and compensated, and thus a realistic facial animation result can be achieved. However, the entire texture updating using traditional waveform encoding methods (such as JPEG, MPEG, etc.) [19, 24] is an expensive approach requiring high bandwidth (bit rates). Guenter *et al.* [12] produced a face by capturing six camera views of high resolution, registered video images of the face and by tracking the geometric deformation using colored circular paper fiducials glued to a person's face. Although the system produced a synthesized face of impressive quality, physical dots had to be glued to a real face, and a large amount of storage space was required for texture mapping. Around a 200 kbits/s bit rate can be achieved while keeping the high quality image, which is, however, not in the range of a very low bit rate transmission (less than 64 kbits/s) [22, 31, 33]. Tao and Huang [35] proposed a piecewise bezier volume deformation model to track face motion; impressive results of the synthesized face expressions were achieved. However, only an initial frame texture was used, the realistic textures (e.g., wrinkles) are still hard to be synthesized as desired for a lifelike expression.

Strom *et al.* [17] coded the entire face texture by employing the classical eigen face approach, which requires a large number of faces as a training set to create a set of eigen textures beforehand (i.e., working offline). Even though the image is divided into small blocks, the complexity of computation is still a major concern in that scheme. In addition, the model adaptation and geometric normalization are performed manually. To achieve a signal-to-noise ratio (SNR) of 35 dB, the bit rate must average over 200 kbit/s, while very low bit rate video coding requires less than 64 kbits/s. Recently, Nishino *et al.* [18] presented a new eigen texture method to make the input image be compressed and stored in eigen space. This method samples appearance of a real object under various illumination and viewing conditions and compresses it in the 2D coordinate system defined on the 3D model surface.

The captured color image is divided into small areas that correspond to triangle patches (called cells) on the 3D model. A sequence of cell images depict appearance variations on the same physical patch of the object from various viewing directions. The compression of the cell image is accomplished using principal component analysis. It can synthesize a virtual object image of a particular pose with high quality by the interpolation method in eigen space and can also seamlessly integrate the virtual object into a real scene. However, no further result of applying this method to motion objects is reported (only static objects look applicable). Moreover the computational expense and a large amount of storage for eigen textures and projection coefficients on the eigen space make it more suitable for applications in which the targets can be compressed offline beforehand; therefore it is not applicable to our online compression system with movable and deformable objects. To alleviate the computational load, some new, less time-consuming, approaches have been investigated recently. A real-time rendering system using the multi-texture mapping method was reported by Kunita *et al.* [23]. The prototype system can synthesize the image at a high spatial sampling density; however, it requires 12 synchronized CCD cameras working together to capture textures simultaneously. Conceivably, more bits are needed to encode such a large number of textures.

In this paper, we propose an efficient method to detect and update the facial textures in active wrinkle areas, and mouth–eye areas, and eventually synthesize the facial expressions using these captured textures to achieve a very low bite rate coding (less than 40 kbit/s). The fiducial point tracking and model adaptation are performed automatically.

Psychology research shows that a significant contribution to a realistic facial expression comes not only from facial organs (i.e., eyes and mouth), but also from facial wrinkles generated from the expression (i.e., expressive wrinkles) [11, 27]. The most significant wrinkles on a human face are categorized into four types: (1) forehead wrinkle; (2) glabella wrinkle (in between the eyebrows); (3) crows-feet wrinkle (outer corners of eyes); and (4) nasolabial wrinkle (below the cheek, linking nose side and mouth corner), as shown in Fig. 2a. In this work, instead of updating the entire facial texture [12, 14, 17, 26], we update only partial textures, defined in the wrinkle areas and mouth–eye areas, which are called *textures of interest* (TOI). Among the TOI, only the significant textures which are generated along with the different expressions are used for image synthesis; they are called *active textures* (AT). To synthesize a realistic facial expression, a wireframe model is first adapted onto the face images to track the movement of expressions. The TOI is estimated based on the fiducial points detected, such as the corners of facial organs and the geometric information. The subsequent facial textures are normalized to an initial frame model, which is taken as a standard size. Before the active textures on the normalized face image are extracted, the TOI with arbitrary shapes are transformed (normalized) to a rectangle shape. Among the normalized TOI, the active textures can be extracted by computing the temporal texture correlation between the current frame and the initial frame. Then the active textures are coded and transmitted to the other side to synthesize the entire facial texture. The principal component analysis method is applied to compress the active textures. To synthesize the facial texture on the receiving side, the first frame texture is mapped onto the subsequent deformed frame model, then the active textures which have been decoded are added onto the corresponding position of the face. A temporal blending technique is used to make the synthesized texture appear more smooth. The system is outlined in Fig. 1. The animation parameters can be compressed by the PCA + DCT compression algorithm presented by Tao *et al.* [34].

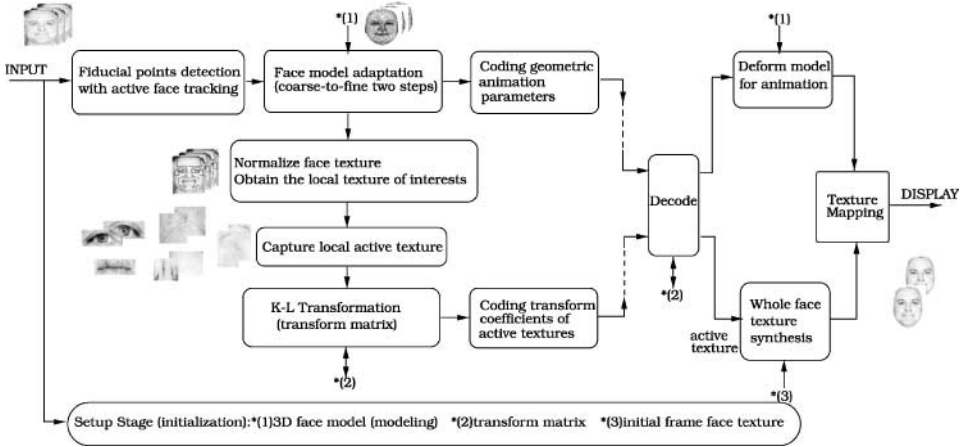


FIG. 1. Flow chart of the system composition.

The remainder of this paper is organized as follows: In Section 2, a method for fiducial point estimation is described; Section 3 explains a new approach for model adaptation. Section 4 shows how to determine the textures of interest and how to detect the active texture area. In Section 5, the active texture compression algorithm is described. Section 6 shows how to synthesize the facial texture with wrinkles for each frame followed by some experimental results with synthesized facial expressions in Section 7. Conclusions and final remarks are given in Section 8.

## 2. FIDUCIAL POINT ESTIMATION

To obtain the textures of interest, a 3D wireframe face model is first matched onto an individual face to track its different facial expressions. The adaptation procedure consists of two stages: facial fiducial point estimation and physics-based dynamic mesh matching. The correct estimation of the facial fiducial points will produce a correct matching of a face model with the face. The accurate matching of the model will lead to an accurate tracking of facial expressions and thus result in a correct selection of textures of interest (e.g., wrinkle textures and eye and mouth textures).

Twenty-seven feature points are defined on a human face, located on the eyebrows, eye corners, nose sides, mouth corners, and hair contour, as shown in Fig. 2a. We developed an active tracking algorithm to estimate the head silhouette [38]. After the head silhouette is obtained, the face and hair areas can be distinguished by a color classifier for their different hue and intensity information; furthermore, a face region growing method is applied to verify the region detected [25]. Thus the border of the face and hair can be obtained. Eye and iris features are typical template-like features which can be robustly estimated by Hough transformation and deformable template [30, 39] exploiting the eye color saturation information [4]. Similarly, mouth shape can be estimated by deformable template methods, using the hue information [38]. Based on the geometrical relationship of eyes and eyebrows, the shape of eyebrows can be estimated by an integration projection method [5]. Nose side is also an important geometric feature in our application, which aids in locating the nasolabial wrinkle area effectively. This feature can be extracted by using a template matching method

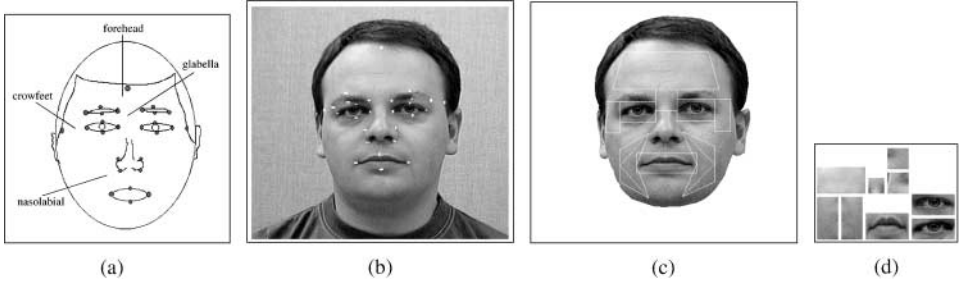


**FIG. 2.** (a) Feature points defined on a human face; (b) An example of feature points extracted on a person's face; (c) textures of interest; (d) Normalization of textures of interest (up: forehead area, glabella area, and left-right crowfeet area; down: left-right nasolabial area, mouth, and left-right eye areas).

[40], in which a statistical correlation estimation between a predefined template and the nose area is applied. After all the feature shapes are extracted, the 27 feature points (corners) distributed on the corresponding shapes can be obtained. Figure 2b illustrates an example of 27 feature points detected on a person's face. We integrated the above existing approaches and developed the system for feature shape detection. Our implementation is described below. (Please see our technique report [37] for a detailed description.)

## 2.1. Facial Organ Features Localization

Analyzing the head image is required to make an estimation of the position and size of the characteristic facial organs, such as eyes, eyebrows, mouth, and nose. Since facial skin, other than facial features and hair, exhibits a similar property in color and luminance, region growing is suitable for extracting the connected skin area, as illustrated in Fig. 3. The whole head region is denoted as  $H$ . The skin region, the subset of  $H$ , is denoted as  $S$ . The feature region is the complementary set of  $S$ , as denoted by  $\bar{S}$ ,  $H = S \cup \bar{S}$ . Determining growing threshold is not a trivial problem because of the small variation of color and luminance in various regions of a face. A large growing threshold produces a large connected skin region, splits the feature region into many pieces, and loses the completeness and shape of the facial features. Moreover, it is difficult to identify and group too many pieces into meaningful facial features. A small growing threshold produces a small skin region and keeps the completeness of facial features. However, sometimes the skin region cannot be completely grown, and when stopped in the middle its incompleteness also causes the failure of facial organ detection. To overcome the difficulties encountered in region growing and make the facial feature detection less sensitive to noise, a two-stage region growing

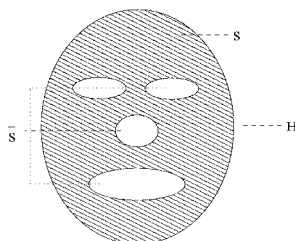


**FIG. 3.** Illustration of skin region and feature region.

algorithm is developed—global region growing and local region growing. In global region growing, a large growing threshold is selected to explore more skin area. Only the most distinct features, such as the darkest parts of the eyes, the nostrils, and in between the lips, remain. These parts provide important information on the locations of the facial features, although the information on the shape and size is lost. The feature region information is estimated in the second-stage region growing (i.e., local region growing). In this stage, the region growing is performed in the feature areas individually. The initial seed pixel of the skin is selected in the local area, and a smaller growing threshold can be selected so that a small skin area surrounding the facial organ is detected and produces as much feature information as possible.

### 2.1.1. Location of Feature Centers Using Global Region Growing

The head silhouette is obtained by background compensation as described in [38], the search of facial features is then limited within this area. In general lighting conditions, the hair and face exhibit distinct color appearances. Also, the facial features of iris, eyebrow, in the between lips, and nostril have a distinguishable darkness when compared with the facial skin, which usually exhibits approximate uniformity in color. Hence, the face feature region can be extracted by segmenting the image using region growing based on the color components. Note that the initial seed for growing is selected randomly in the face region; the size of the grown region must be checked to ensure that it will be a reasonable face region (e.g., the size must fall in between the half size of the silhouette area and the full size of the silhouette area). As long as the size of the grown region is not of a reasonable size, the seed must be reselected (e.g., neighbor pixel). The iteration process is performed until the grown region fulfills the predefined condition. After the skin region growing, a number of regions (blobs) are obtained. To extract the facial organ blobs (e.g., eyes, mouth, nose, etc.), the top blobs and the bottom blobs (e.g., hair, collar, cloth, etc.) are removed. The feature blobs are then processed for further classification by using  $k$ -means classifier.

Note that the eyebrow is also included in the eye class, their separation will be done later in the shape estimation section. After the four feature classes are obtained, the *class center* for each feature class can be obtained by taking the average of all blob centers of that class. Figure 4 shows some examples of feature estimation.

### 2.1.2. Location of Feature Regions Using Local Region Growing

The local area of each feature (organ) is determined by the estimated location of the feature center and the predefined surrounding size. To grow a skin region in the local area, a seed pixel is selected from the periphery skin area of the feature organ. A smaller growing



**FIG. 4.** Classified features (the regions in the same class are labeled by the same gray level; the bottom terminal of each vertical line is the center of each feature).



FIG. 5. Extracted feature blobs.

threshold  $D_{T_s}$  is predefined. The feature blobs with large area are created, based only on the luminance of the image rather than three color components. The feature region is a complementary set of the grown region within a surrounding window. Finally the region size of each organ (called the *organ window*) can be derived from the extracted feature blobs which are represented by a binary image  $\mathbf{b}$ . The feature area is represented by a high value while the background area is represented by value zero, as shown in Fig. 5.

Note that the nose window and the eye window may be partially overlapped. In that case, the nose window can be adjusted by shrinking in the vertical direction. This adjustment prevents the class boundaries from overlapping. Eventually, feature areas with clear boundaries can be obtained, as shown in Fig. 6.

## 2.2. Shape Estimation

The above work shows how facial features are restricted in the corresponding windows. The next stage is to extract the real shape for fiducial point localization and the model adaptation. The shape of facial features mainly refers to the contour of eye, eyebrow, mouth, nose (nostril and nose side), and chin.

We choose deformable template using color information to detect the feature shapes. The approaches to detecting eyes and mouth are similar; both use deformable template matching and exploit color information. In addition, eye detection uses the Hough transform to search the iris position and size to determine the initial location of the eye template.

### 2.2.1. Detection of Eye Shape

The approach to detecting the eyes is similar to [7] in that it uses the Hough transform and deformable template matching; however, it also exploits color information (saturation) to extract the eyes accurately. Since the coarse regions of two eyes have been robustly detected in the previous section, the iris searching range is greatly reduced. The iris is the most significant feature of the eye and has a simple circular shape. It is detected first by using a gradient-based Hough transform for circles [8, 21].



FIG. 6. The restricted window area based on the extracted feature blobs.

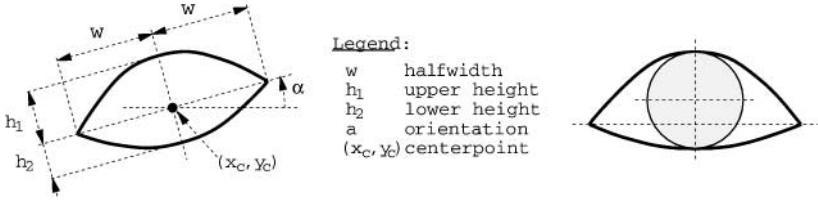


FIG. 7. Deformable template (model, initialization).

After the circles are extracted the deformable templates for the eyelids have to be initialized. The model, along with all the parameters used, is shown in Fig. 7, with the parameters being set as

$$h_1 = 1.5r_{iris} \quad h_2 = 0.5r_{iris} \quad w = 2.2r_{iris}, \quad (1)$$

where  $r_{iris}$  is the radius of the extracted circle. The orientation  $\alpha$  is determined by the center points of the two circles. The initialized deformable template is also shown in Fig. 7. To avoid the shrink problem, the location of the template and the size of the template are determined separately. Two different types of image information are used to create potential fields, one in each epoch. The image information extracted from a typical eye is shown in Fig. 8. First, the color information (saturation) is exploited to locate the eyelids by approximating the position of the deformable template relative to the iris. This is done by minimizing the following energy ( $E_{sat}$ ), which is similar to the valley energy in [39],

$$E_{sat} = -\frac{1}{|A_w|} \int_{A_w} \Phi_{sat}(\vec{x}) dA. \quad (2)$$

$A_w$  is the area inside the parabolas but not inside the circle of the iris, and  $\Phi_{sat}(\vec{x})$  is the inverted saturation value of the color image. Since only the location (not the size) is changed this method does not have the shrinking effect.

Next, the deformable template is matched accurately to the eyelids by minimizing the following energy ( $E_{edge}$ ):

$$E_{edge} = -\frac{1}{|B_w|} \int_{B_w} \Phi_{edge}(\vec{x}) ds. \quad (3)$$

$B_w$  is the boundary of the parabolas and  $\Phi_{edge}(\vec{x})$  is the edge magnitude. During this minimization every parameter of the deformable template (location, orientation, height,



FIG. 8. Image fields used for computing the potential energy (image, saturation, edge).



**FIG. 9.** Sequence (sample frame 1, 24, 68, 169) showing eye movement with matched eye template.

and width) can be changed. Some sample frames with the detected iris and lids' shape are shown in Fig. 9.

### 2.2.2. Detection of Eyebrow

Notice that in the feature location stage described in the previous section, the eyebrows and eyes sometimes are difficult to separate because of the connection of the regions. Thus in that stage, these two features are not distinguished; instead the eye regions detected contain the eyebrow region. Because the iris and eye shape have been extracted by the deformable template technique, the eye area can be excluded from the set of eye class, the remaining set is the eyebrow area. The eyebrow has a distinguishable dark luminance from the surrounding skin. The integral projection from horizontal and vertical directions can be used respectively for a good shape estimation of the eyebrow.

The integral projection is a very useful technique for the extraction of regional salient features [5]. Projections can be effective in determining the position of features. Let  $P(x, y)$  be an image patch which contains the object of interest. The vertical integral projection of  $P(x, y)$  in the  $[x_1, x_2] \times [y_1, y_2]$  rectangle is defined as

$$IV(x) = \sum_{y=y_1}^{y_2} P(x, y). \quad (4)$$

The horizontal integral projection is similarly defined as

$$IH(y) = \sum_{x=x_1}^{x_2} P(x, y). \quad (5)$$

Since we have detected the eye shape, the approximate eyebrow region can be determined using anthropometric measure (geometric relation of the eye and eyebrow). In the delimited window of the eyebrow, the eyebrow width is computed by using the vertical integral projection of the intensity and finding the two most significant opposite gradients in the projection, the leftmost and rightmost points of the eyebrow can be detected.

To estimate the shape of the eyebrow, the horizontal integral projection is applied to each column from the leftmost eyebrow to the rightmost eyebrow. The projection in each column produces two most significant opposite gradients, whose positions are detected for estimating the height of the eyebrow at that column. The estimated column height and the position form the entire shape of the eyebrow. The example of the eyebrow detection is shown in Fig. 10.

### 2.2.3. Detection of Mouth Shape

The algorithm for mouth detection can be outlined as follows:



**FIG. 10.** Example of the eyebrow shape extraction using integral projection (IP): (left) horizontal IP is applied within the vertical window. The left part of the graph is the curve of  $IH(y)$ ; (middle) vertical IP is applied within the horizontal window. The lower part of the graph is the curve of  $IV(x)$ , in which the two locations with maximum opposite gradients correspond to the two ends of the eyebrow; (right) shape extraction using horizontal IP in each column.

- Determine a coarse region of interest for the mouth, and determine the mouth status: *closed* or *open*.
- Using color information (*hue* component) get an initial approximation for the lip. This is done by minimizing the energy cost function.
- Localize the mouth contour by minimizing the edge cost function.

The features of the mouth are described by an open-mouth template and a closed-mouth template, separately, which are composed of four or three parabolas  $P_i$ , respectively, as shown in Fig. 11. The mouth features are represented by the mouth corner points and the thickness of the lips. The open-mouth template consists of four parabolic curves, which are defined as

$$p_i = h_i^o \left( 1 - \left( \frac{q}{L_M} \right)^2 \right), \quad (6)$$

where the parameters  $h_i^o, i = 1, 2, \dots, 4$ , described opening heights of the upper and lower lips. The width of the mouth  $L_M$  is calculated as the distance between the two corners of the mouth. The thickness of the lips are calculated as  $|h_1^o - h_2^o|$  and  $|h_4^o - h_3^o|$ . To represent an open-mouth feature, six parameters are needed:  $h_i^o, i = 1, 2, \dots, 4$ , and the two corners of the mouth  $m_l$  and  $m_r$ .

The closed-mouth template consists of three parabolic curves, which are defined as

$$p_i = h_i^c \left( 1 - \left( \frac{q}{L_M} \right)^2 \right). \quad (7)$$

To represent a closed-mouth feature, five parameters are needed:  $h_i^c (i = 1, 2, 3)$  and the two corners of the mouth  $m_l$  and  $m_r$ .

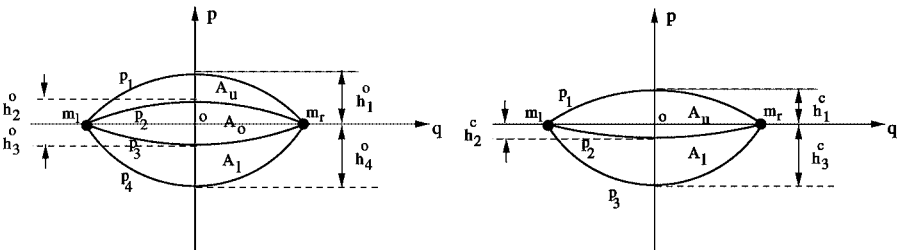


**FIG. 11.** Deformable template for open mouth (left) and closed mouth (right).

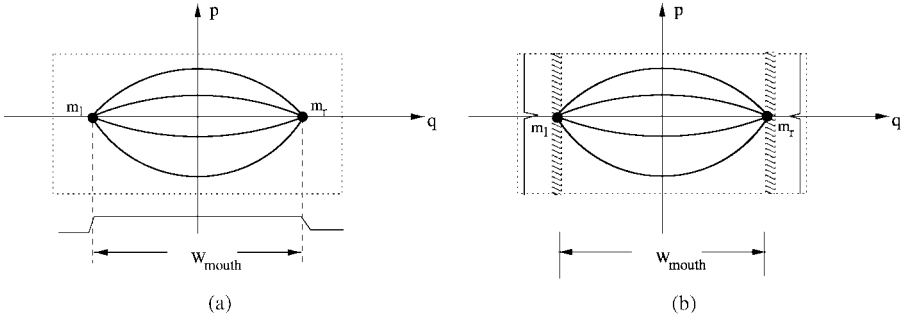


**FIG. 12.** Determination of the corners of a mouth: (a) Vertical projection for determining the width of a mouth. (b) Horizontal projection for determining the corners of a mouth.

(1) Determination of mouth corners: In the previous section, the region center of the mouth has been estimated. Using the vertical integral projection of the hue component of the mouth region, two vertical lines at the leftmost and rightmost corners of the mouth can be determined by finding the two most significant opposite gradients in the projection (Fig. 12a). Suppose that the orientation of the mouth (i.e., a line in between the lips) follows the orientation of the eye (i.e., a line connecting the centers of the left eye and the right eye). At both sides, the horizontal integral projection, along the orientation of the mouth, is performed to find the local peak for determining the location of the mouth corner (Fig. 12b). The example of the estimation of mouth corners is shown in Fig. 13.

(2) Determination of closed mouth and open mouth: Because there are two deformable templates, an open-mouth template and a closed-mouth template, the situation of whether the mouth is open or closed has to be determined first. When considering the situation in color space, the lips present a distinctive color property from the other areas of the mouth. In a vertical strip crossing the center of the mouth, the horizontal integral projection of the hue component appears as two peaks in the projection map. The width of the valley of the horizontal projection is a rule for discriminating whether the mouth is open or closed. If the width of the valley is beyond two pixels, the mouth is assumed to be open; otherwise, the mouth is assumed to be closed (see Figs. 14 and 15). The width of the valley is estimated to be an initial parameter for the open-mouth template (i.e.,  $h_2^o + h_3^o$ ). The distance between the two most significant opposite gradients of the outside valley is estimated as the initial parameter of the lip distance (i.e.,  $h_1^o + h_4^o$ ).

(3) Deformable template matching: After it has been determined whether the mouth is open or closed, deformable template matching can be performed to select the initial parameters from the valley position. For instance, the initial parameter for the height of the outside upper lip  $h_1^o$  is calculated as the distance from the upper edge of the outside

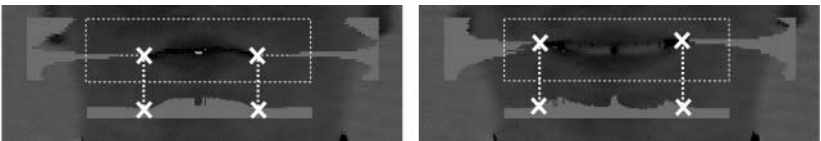


**FIG. 13.** Example of the mouth corner estimation.

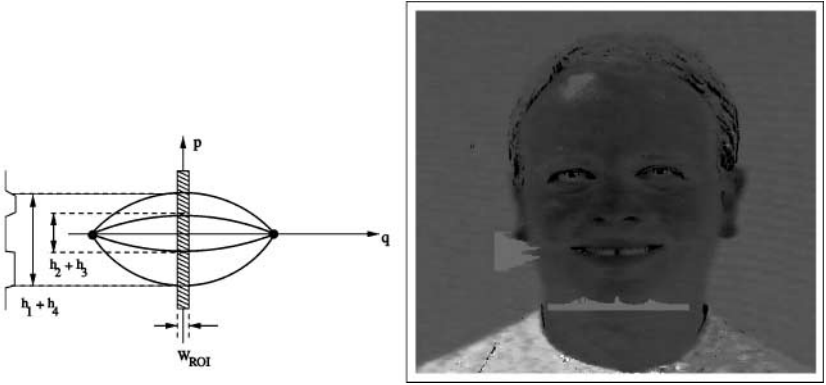


**FIG. 14.** Integral projection of the hue component for a mouth: (left) Horizontal projection to determine the mouth—closed and mouth—open; (right) an example.

valley to the mouth center, while the one for the inside upper lip  $h_2^o$  is the distance from the upper edge of the inside valley to the mouth center. A similar procedure is followed for the estimation of the initial parameters  $h_3^o$  and  $h_4^o$ .

In the case of mouth closed, the initial parameter of  $h_2^o$  is estimated as the distance from the lower edge of the valley to the mouth center.

For the template matching in two different situations (i.e., mouth open and mouth closed), different cost functions are proposed to deal with each case.

• **Mouth-open cost function:** The first cost function for an open mouth  $E_1^o$  is based on the color information of the lips, which is defined as

$$E_1^o = k_1 E_{hue}^o + k_2 E_{mean}^o + k_3 E_{var}^o, \quad (8)$$

where

$$E_{hue}^o = \frac{1}{|A_u|} \int_{A_u} \Phi_{hue}(\vec{x}) dA + \frac{1}{|A_l|} \int_{A_l} \Phi_{hue}(\vec{x}) dA \quad (9)$$

$$E_{mean}^o = -|m_{A_u} - m_{A_o}| - |m_{A_l} - m_{A_o}| + \sigma_{A_u} + \sigma_{A_o} + \sigma_{A_l} \quad (10)$$

$$E_{var}^o = |\sigma_{A_u} - \sigma_{A_o}| + |\sigma_{A_o} - \sigma_{A_l}| + |\sigma_{A_l} - \sigma_{A_u}|, \quad (11)$$

where  $A_u$  and  $A_l$  are the areas inside the parabolas of the upper lip and the lower lip, respectively;  $\Phi_{hue}(\vec{x})$  is the value of the hue component of the mouth image. Since the lips appear more red under common lighting conditions, the hue component of the lip regions is usually small.  $m_{A_u}$ ,  $m_{A_l}$ ,  $m_{A_o}$  and  $\sigma_{A_u}$ ,  $\sigma_{A_o}$ ,  $\sigma_{A_l}$  are the means and the variances of the hue



**FIG. 15.** Example of the horizontal projection of hue component for mouth—closed/open.

component of the image in the regions of  $A_u$ ,  $A_l$ , and  $A_o$  (in between the lips), respectively. Since the teeth and the rest of the region between the lips have very different values in the  $Y$  (luminance) component but not in the hue component, the hue component is used here for evaluation rather than the  $Y$  component. Coefficients  $k_i$  ( $i = 1, 2, 3$ ) are the weighting factors, which were set to 1 in the experiments, so that the three energy terms are treated equally in their contribution to the calculation of the cost function. The second term  $E_{mean}^o$  considers that the regions  $A_u$ ,  $A_l$ , and  $A_o$  have different hue values but inside each region there are almost no differences in hue value. The third term  $E_{var}^o$  considers that the variance of the camera noise is the same in all regions. The deformable template matching in this step is done by minimizing the energy  $E_1^o$ ; the combination of  $(h_1^o, h_2^o, h_3^o, h_4^o)$  with the minimum value of  $E_1^o$  is selected as the approximate lip outline parameters of the open mouth.

To match the deformable template accurately to the mouth shape, the four curves are further tuned by minimizing the following edge energy:

$$E_2^o = - \sum_{i=1}^4 \frac{1}{|B_{p_i}|} \int_{B_{p_i}} \Phi_{edge}(\vec{x}) ds. \quad (12)$$

$B_{p_i}$  ( $i = 1, 2, 3, 4$ ) are the boundaries of the parabolas and  $\Phi_{edge}(\vec{x})$  is the edge magnitude.

• **Mouth-closed cost function:** The cost function for a closed mouth is similar to the case of the open mouth, except that no  $A_o$  area appears in the closed mouth,

$$E_1^c = k_1 E_{hue}^c + k_2 E_{mean}^c + k_3 E_{var}^c, \quad (13)$$

where  $E_{hue}^c$  is same as  $E_{hue}^o$

$$E_{mean}^c = |m_{A_u} - m_{A_l}| + \sigma_{A_u} + \sigma_{A_l} \quad (14)$$

$$E_{var}^c = |\sigma_{A_l} - \sigma_{A_u}|. \quad (15)$$

Coefficients  $k_i$  ( $i = 1, 2, 3$ ) are the weighting factors, which are set to 1 in the experiments.

After the region energy  $E_1^c$  for the closed mouth is minimized, the parameters of the template are further tuned by minimizing the edge energy, which is similar to the case of the open mouth; i.e.,

$$E_2^c = - \sum_{i=1}^3 \frac{1}{|B_{p_i}|} \int_{B_{p_i}} \Phi_{edge}(\vec{x}) ds. \quad (16)$$

$B_{p_i}$  ( $i = 1, 2, 3$ ) are the boundaries of the parabolas and  $\Phi_{edge}(\vec{x})$  is the edge magnitude. Some sample results are shown in Fig. 16.

#### 2.2.4. Detection of Nose Shape

The important nose features lie in the shapes of nostril and nose side. The accurate shape of the nostril and the nose side can be an important component in a facial expression; especially when a person is smiling or laughing, the nostril shape and the nose side change.



FIG. 16. Sample frames of the deformable template matching on open/closed mouths.

(1) Nostril estimation: The nostril has a distinctive darkness from the facial skin. As mentioned in the previous section, color-based region growing can roughly detect the position and the approximate shape of the nostrils. To detect the nostril shape correctly, a geometric template is further applied to the nostril region, which is a twisted pair curve with a leaf-like shape, as shown in Fig. 17. The nostril template is defined as a part of a twisted pair curve, which is represented in a polar coordinate system,

$$\rho^2 = a^2 \cos(s\theta). \quad (17)$$

The nostril on the right side and the left side of a nose can be represented by the up-right curve and the up-left curve, respectively. Parameter  $a$  is the width of a nostril. Parameter  $s$  controls the shape of the curve, which is a real number in the range of  $[1, 10]$ . The smaller the  $s$  value, the thicker the leaf-shape appears. Besides the parameters  $a$  and  $s$ , the orientation of the  $x$  axis and the position of the origin  $o$  can be adjustable as well. The relationship

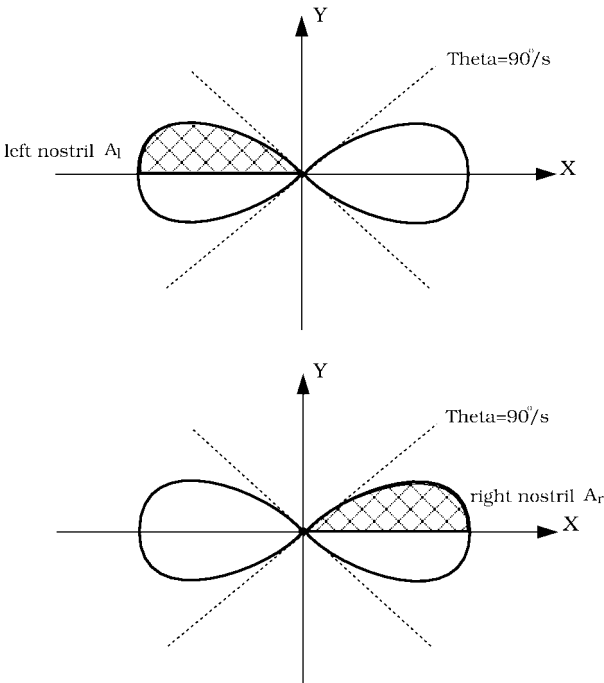


FIG. 17. Template of nostrils.

between  $(x, y)$  in Cartesian coordinate system and  $(\rho, \theta)$  in polar coordinate system is simply defined as

$$x = \rho \cos(\theta) \quad (18)$$

$$y = \rho \sin(\theta). \quad (19)$$

From the detection of the nose regions in the previous section using color-based region growing, the initial width of the nostril can be determined by calculating the distance between the leftmost and rightmost pixels in the nostril region. The initial orientation of the nostril can be determined by the eigen vector with the largest eigen value of the nostril pixel region. The initial shape control parameter  $s$  is set to the value 2. Note that the two nostrils are assumed to be symmetric with respect to the center line of the face; the nostril not detected in the first stage can be determined by flipping the previous template.

After the initial parameters are estimated, deformable template matching can be performed with the cost function for energy minimization being defined based on the assumptions that: (1) the nostrils have distinctive darkness compared to the skin and (2) the luminance gradient has a high value at the border of a nostril. The cost function for the right nostril is defined as

$$E^{nl} = k_1 E_{lumin}^{nl} + k_2 E_{grad}^{nl}, \quad (20)$$

with  $E_{lumin}^{nl}$  being

$$E_{lumin}^{nl} = \frac{1}{|A_r|} \int_{A_r} \Phi_{lumin}(\vec{x}) dA \quad (21)$$

and  $E_{grad}^{nl}$  being

$$E_{grad}^{nl} = -\frac{1}{|B_r|} \int_{B_r} \Phi_{grad}(\vec{x}) ds. \quad (22)$$

$A_r$  is the area inside the up-half of the right leaf-shape curve.  $\Phi_{lumin}(\vec{x})$  is the value of luminance component of the nostril region.  $\Phi_{grad}(\vec{x})$  is the edge magnitude.

The cost function for the left nostril has the same definition as that for the right nostril, except the left leaf-shape curve is used instead. During this minimization every parameter of the deformable template (location, orientation, width, and shape) can be changed.

(2) Nose side estimation: The nose side is shaped like a vertical parabola. Assume that the nose orientation has been normalized into the straight direction which is parallel to the face center line, a pair of templates of the nose side (both the right and left sides) are defined in Fig. 18:

$$x_l = \left( h_{ls} \left( 1 - \left( \frac{y_l}{|n_{l2} - n_{l1}|} \right)^2 \right) \right) \quad (23)$$

$$x_r = \left( h_{rs} \left( 1 - \left( \frac{y_r}{|n_{r2} - n_{r1}|} \right)^2 \right) \right). \quad (24)$$

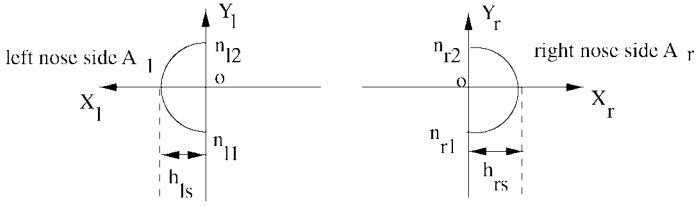


FIG. 18. Template of the nose side.

The initial corner of the nose side  $n_{l1}$  and  $n_{r1}$  have been fixed since the nostril has been estimated. The parameter  $n_{l2}$ ,  $n_{r2}$  and the width  $h_{ls}$ ,  $h_{rs}$  need to be estimated by minimizing the energy, as defined below—the cost function for the right side of a nose

$$E^{ns} = k_1 E_{lumin}^{ns} + k_2 E_{grad}^{ns}, \quad (25)$$

with  $E_{lumin}^{ns}$  being

$$E_{lumin}^{ns} = -\frac{1}{|A_r|} \int_{A_r} \Phi_{lumin}(\vec{x}) dA \quad (26)$$

and  $E_{grad}^{ns}$  being

$$E_{grad}^{nl} = -\frac{1}{|B_r|} \int_{B_r} \Phi_{grad}(\vec{x}) ds. \quad (27)$$

$A_r$  is the area inside the parabola, which has bright luminance value  $\Phi_{lumin}(\vec{x})$  in the nose wing.  $\Phi_{edge}(\vec{x})$  is the edge magnitude.

The cost function for the left side of a nose has the same definition as that for the right side. In the course of nose tracking, the parameters obtained from the previous frame can be also used as the initial parameters of the nose template in the current frame. Some sample frames with the detected nostril and nose sides are shown in Fig. 19.

### 2.2.5. Detection of Chin Contours

For an automatic analysis of the person's facial expressions, a more accurate adaptation of the face model to the chin contours of the individual person is necessary. Therefore, the chin contours in the image sequence have to be estimated.



FIG. 19. Sample frames of the deformable template matching on nostril and nose sides.

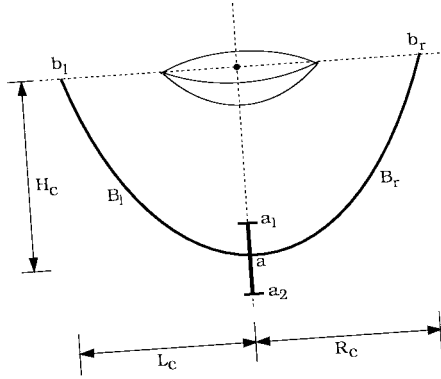


FIG. 20. Deformable template of a chin.

The geometric model of the chin region simply consists of two parabolas (see Fig. 20). The energy function is relatively simple:

$$E^{chin} = k_1 E_{symm}^{chin} + k_2 E_{grad}^{chin}. \quad (28)$$

The first term is based on the assumption that the chin has a symmetric structure with respect to face vertical center,

$$E_{symm}^{chin} = [L_c - R_c]^2. \quad (29)$$

The second term  $E_{grad}^{chin}$  is the gradient energy in the chin boundary,

$$E_{grad}^{chin} = -\frac{1}{|B_r|} \int_{B_r} \Phi_{grad}(\vec{x}) ds - \frac{1}{|B_l|} \int_{B_l} \Phi_{grad}(\vec{x}) ds. \quad (30)$$

The initial endpoints  $b_l$  and  $b_r$  can be determined by the intersection of the facial silhouette and the orientation of mouth horizontal, both of which have been estimated in the previous section. The chin bottom point  $a$  must occur at a certain position between  $a_1$  and  $a_2$  with respect to the original mouth center, empirically based on the anatomy of an average face; i.e.,

$$a_1 = |center_{nose} - center_{mouth}|/2 + center_{mouth} \quad (31)$$

$$a_2 = |center_{nose} - center_{mouth}| \times 2 + center_{mouth}. \quad (32)$$

During the energy minimization, only the positions  $b_l$ ,  $b_r$ , and  $a$  are adjustable. Some examples of chin contour detection are shown in Fig. 21.



FIG. 21. Sample frames of the deformable template matching on chin contours.

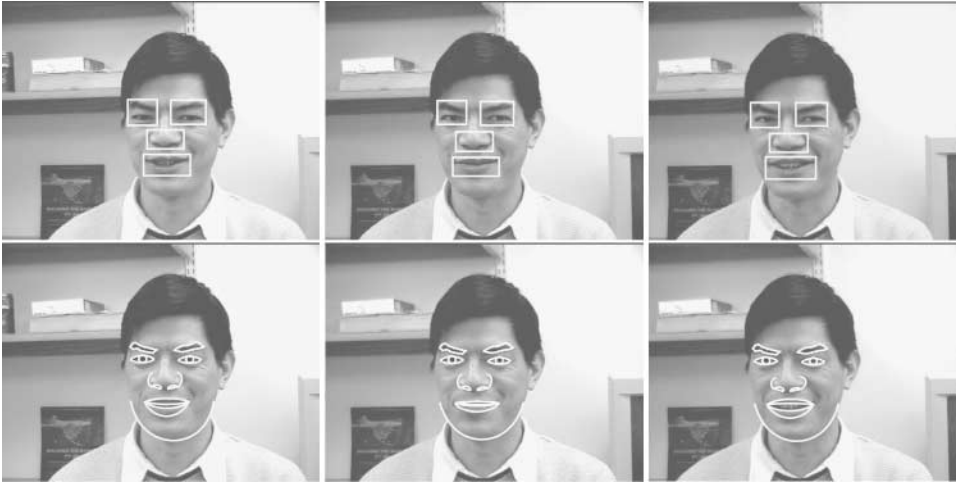


**FIG. 22.** Top: coarse regions detected by color-based two-step region growing; Bottom: detected facial features (iris, eye, eyebrow, nostril, nose sides, mouth, and chin) on frames 10, 24, 41 of video sequence “Guan.”

### 2.3. Performance Evaluation

We tested the feature detection algorithm on several other video sequences; Fig. 22 is the sample result of video “Guan.” The integration of active tracking and two-stage region growing limits the feature searching area and, furthermore, increases the efficiency of the template initialization. Thanks to the ability of the selectable region “seeds,” the region restriction is made effectively. As shown before, the deformable template incorporating color information and integral projection detected the facial feature correctly. However, some moderate assumptions are imposed in our work, which is similar to most existing work, such as:

- The input images are a sequence of images showing the head and shoulders of a person talking in front of a camera.
- The motion of the speaker is moderate with respect to the frame rate (and image size).
- Certain facial features are always visible. Thus, head rotations that impede the visibility of eyes and mouth are excluded. Similarly, the face may not be occluded by other objects such as gesticulating hands.
- The head inclination (rotation around the three main axes  $x, y, z$ ) is less than 45 degrees.
- The face has no facial hair (such as a beard or a moustache), glasses, etc.

We use a camera mounted on an active platform (pan/tilt) to take an active video sequence, which shows a talking person with an unconstrained background. The camera rotation is less than  $\pm 5^\circ$ . In the eye tracking, the Hough transform coupled with the saturation-based deformable template is the first important step to extract the eye shape. The hue information is explored for lip shape extraction. The closed-mouth and open-mouth detection gives us sufficient accuracy to use the corresponding template to match to the mouth. The extraction of the chin, nostril, and nose side has been attempted as well in this section. Note that our deformable template matching algorithm only uses several single steps to fit the template to the facial features, it avoids the computational complexity resulting from a large amount of search of the parameters, and the template shrinking problem.

**TABLE 1**  
**Performance Evaluation of the Detection of Facial Features in Eight Video Sequences**

Sequence title	Number of tested frames	Absolute mean deviation (in pixels)					
		eye(l/r)	eyebrow(l/r)	noside(l/r)	nostril(l/r)	mouth	chin
Mario	60	1.9/2.0	2.1/1.9	1.8/2.0	2.1/1.9	2.8	3.0
Guan	30	2.1/1.8	1.8/1.8	1.7/1.9	1.6/2.0	3.0	3.4
Dima	30	3.4/3.8	1.8/1.4	2.1/2.0	1.5/1.9	2.9	3.8
Stan	30	3.3/3.5	2.5/2.2	2.0/1.7	1.9/2.2	4.0	5.1
Dana	30	2.5/3.0	2.3/2.5	2.3/2.7	2.0/1.8	3.7	3.5
Xun	30	3.2/3.6	3.1/2.9	3.0/2.8	3.0/2.4	2.5	3.2
Claire	30	1.2/1.3	2.4/2.7	2.8/2.3	1.4/1.4	2.9	2.7
Alau	30	1.5/1.4	1.3/2.1	1.4/1.9	1.8/1.6	2.3	2.3
<i>Total</i>	<i>270</i>	<i>2.4</i>	<i>2.1</i>	<i>2.1</i>	<i>1.9</i>	<i>2.9</i>	<i>3.3</i>

*Note.* l/r stands for left/right. Sample frames from these video sequences are shown in Fig. 23.

The feature tracking algorithm is also tested on other video sequences (such as “Dima,” “Stan,” “Dana,” “Xun”) with pan and tilt movement of the active platform, and with still camera platform (such as “Claire,” and “Alau”). The performance for detecting the feature objects is shown in Table 1. The sample frames of the eight video sequences are shown in Fig. 23. The features of objects are considered being correctly detected if the feature points of the



**FIG. 23.** From top left to bottom right: Mario, Guan, Dima, Stan, Dana, Xun, Claire, and Alau. In each box: original frame (left); feature shape detected (right).

corresponding region falls close enough to the manually determined points in each frame (i.e., the distance between the detected point and the manually picked point should be less than 4 pixels). Table 1 indicates for each sequence: the number of frames tested, the absolute mean error in the feature regions of the eye, eyebrow, nose side, nostril, mouth, and chin. The overall performance (measured over all tested frames) gives an indication of the capability of the system to detect most feature objects correctly (only 18 of 270 frames have an indication that the position errors in mouth, nose side, eyebrow, and chin regions are beyond 4 pixels). The reasons for the failure are: (1) initial template localization is not accurate enough if the head rotation is large (such as “Xun” and “Dima”); (2) the hue and saturation signals are not strong enough under certain imaging conditions (such as “Stan,” “Dima,” and “Dana”); (3) the size of the feature area appears small if the image resolution is low (such as “Claire”  $288 \times 360$  pixels) and cannot provide enough feature information for template matching.

The feature extraction proposed here is, to some extent, invariant under changing lighting conditions. However, when these changes drastically influence the object region’s image characteristics (e.g., when there is an artificial edge in image due to shadowing effects), the shape extraction scheme may find an incorrect shape. Changes in scale, rotations, and lighting conditions or occlusions may cause a mismatch between the assumed image characteristics and the actual characteristics and thus influence the performance of the shape extraction scheme. Therefore, a more flexible and adaptive template needs to be designed so that the multiple templates for one object region or a higher order template can be used for improving the performance of feature extraction. Future research should mainly be directed toward improving the robustness and accuracy of the shape extraction scheme. We have the following suggestions to accomplish this:

- The template which is used in a given situation should be predictable on the basis of the information extracted from the coarse region, so that different templates for various imaging conditions can be introduced.
- In the current implementation, parabolic boundary curve templates are used for feature shape estimation, such as eye contours, lip shape, etc., which mostly use three parametric curves with three control points for each boundary curve (i.e., two endpoints and one middle point). To increase the accuracy of the template matching, the old template model can be improved by increasing the order of each boundary curve, through adding more control points to each outline curve, which is a so-called “fine-tuned template.”

### 3. PHYSICS-BASED DYNAMIC MESH MATCHING

Using the information extracted from head motion [38] and facial features (i.e., fiducial points, eye contour, mouth contour, and face silhouette), a 3D wireframe model can be fitted to the moving face. We developed a so-called “coarse-to-fine” adaptation algorithm using the extended dynamic mesh to implement the model adaptation procedure. The principle of the extended dynamic mesh is to minimize the mesh energy, which is stored in nodal points, based on the features of images. Dynamic mesh (DM) (or called adaptive mesh) is a well-known approach for adaptive sampling of images and physically based modeling of non-rigid objects. The results shown by previous work [13, 20, 36] demonstrated that this technique has become the basis for many powerful approaches in computer vision and computer graphics. The adaptive mesh can be assembled from nodal points connected by

adjustable springs. The fundamental equation [13] is a second-order differential equation, which can be written as

$$m_i \frac{d^2 \mathbf{x}_i}{dt^2} + \gamma_i \frac{d\mathbf{x}_i}{dt} + \mathbf{g}_i = \mathbf{f}_i; \quad i = 1, \dots, N, \quad (33)$$

where  $\mathbf{x}_i$  is the position of node  $i$ ,  $m_i$  is the point mass of node  $i$ ,  $\gamma_i$  is the damping coefficient dissipating kinetic energy in the mesh through friction,  $\mathbf{f}_i$  is the external force acting on node  $i$ , and  $\mathbf{g}_i$  is the internal force on node  $i$  due to the springs connected to neighboring node  $j$ .

To simulate the dynamics of the deformable mesh, the equations of motion are numerically integrated forward through time until the mesh is *nearly* stabilized. Although a number of numerical methods to solve this equation have been used (e.g., Euler method and Runge–Kutta method [29, 36], the stability is still the main concern in achieving a satisfactory solution. For example, when a node moves across an image feature boundary associated with an abrupt change in its image intensity, the stiffness of those springs connecting with the node changes rapidly and results in a possible reversal of the nodal force, which may lead to perpetual oscillation of the node. In this type of situation a new equilibrium state cannot be reached. To make the mesh converge to a stable state,  $m_i$  and  $\gamma_i$  must be carefully chosen. The overdamped behavior (i.e., large values of  $m_i$  and  $\gamma_i$ ) will contribute to enhancing the stability of the numerical simulation; however, it is at the expense of the accuracy of the solution. To make the solution more stable and accurate, we extend the conventional dynamic mesh method [13] by introducing a so-called “energy-oriented mesh” (EOM) to refine adaptive meshes. The major differences between conventional dynamic mesh and the EOM are: (1) EOM makes the mesh movement in the direction of mesh energy decrease instead of decreasing the node velocities and accelerations and (2) EOM checks the node energy in each motion step without considering the velocity it is independent of the DM and can be the supplemental step to the DM for stabilizing mesh movements. Therefore, our model adaptation procedure consists of two major steps: (1) coarse adaptation, which applies the DM method to make the large movement converge quickly to the region of an object and (2) fine adaptation, which applies the EOM method to finely adjust the mesh obtained after the first step and make the adaptation more “tight” and “accurate.”

### 3.0.1. Principle of Energy Minimization in Energy-Oriented Mesh

According to the principle of minimum potential energy, of all possible kinematically admissible displacement configurations that an elastic body can take up, the configuration which satisfies equilibrium makes the total potential energy assume a minimum value [9]. The potential energy stated in the principle of minimum potential energy includes the strain energy and the potential energy formed by external forces. In our model, there is no external force and all the strain energy is stored as the elastic energy in springs. To reach the equilibrium state, the elastic energy in the springs have to be minimized by displacing nodes. If we let node  $i$  move under a nodal force while all the neighboring nodes are fixed, the node will move in the direction of the nodal force because the gradient of total spring energy on node  $i$  ( $E_i$ ) is in the same direction as the nodal force ( $\mathbf{g}_i$ ). This implies that for meshes associated with the image observations, if we let nodes move by successive steps based on the principle of minimum potential energy and reduce strain energy at each step, finally we should obtain a fine adaptation of this image.

When a spring mesh is not in equilibrium state, those nodes with non-zero forces acting on them tend to move in the direction of the resultant nodal forces. The movements of nodes will reduce the energy caused by strain. When a final equilibrium state is reached, no further movements will occur. To prevent a node from being over displaced at each step, energy change for each step must be checked to ensure that the step has reduced the energy in a non-increasing way along the direction of movement.

### 3.0.2. Detailed Algorithm

We use a detailed 3D face model (2954 vertices and 3118 patches) to achieve more realistic animation. The following is the main procedure for the face model adaptation:

I. Based on the 3D face model, feature vertices can fit to the feature points directly; the feature points consist of fiducial points, eye contour, mouth contour, and face silhouette, which are extracted in the previous stage.

II. To adapt the remaining vertices (i.e., non-feature vertices) onto the face image, two steps are applied: (1) coarse adaptation (DM method) and (2) fine adaptation (EOM method).

(1) Coarse adaptation: Solve the dynamic motion equation (33) using conventional explicit Euler time-integration procedure [29] until the motion parameters (velocity  $\mathbf{v}_i$  and acceleration  $\mathbf{a}_i$ ) are less than a certain threshold. In our implementation of Eq. (33) no external force is involved. The boundary vertices are fixed, which include the *feature vertices* defined on the face model and the *vertices on the border* of the face silhouette. Let node  $i$  be connected to a set of nodes (denoted by  $M_i$ ). The set  $M_i$  contains  $n_i$  nodes; i.e., node  $i$  is attached to  $n_i$  springs. The total internal force acting on node  $i$  due to these spring movements is

$$\mathbf{g}_i = \sum_{j \in M_i} C_{ij} (\|\mathbf{r}_{ij}\| - l_{ij}) \frac{\mathbf{r}_{ij}}{\|\mathbf{r}_{ij}\|}, \quad (34)$$

where  $\mathbf{r}_{ij} = \mathbf{x}_j - \mathbf{x}_i$ ,  $\mathbf{x}_i$ , and  $\mathbf{x}_j$  are the positions of nodes  $i$  and  $j$ ;  $l_{ij}$  is the natural length of the spring connected from nodes  $i$  to  $j$ ;  $\|\mathbf{r}_{ij}\|$  is its actual length; and  $C_{ij}$  is the stiffness of the spring  $ij$ .

Based on the nodal value (i.e., intensity in the nodal position), the springs automatically adjust their stiffness to distribute meshes in accordance with the local complexity of the image. Before calculating the stiffness, we apply a Sobel operator to obtain a gradient image, then normalize the intensity values of the gradient image within the range of  $[0, 1]$ . Suppose the stiffness of a spring changes linearly along with the nodal values on the normalized gradient image, the calculation is then

$$C_{ij} = -(k_2 I + k_1), \quad (35)$$

where  $k_1$  is the predefined minimum stiffness of springs in the mesh;  $k_1 + k_2$  is the maximum stiffness of springs; and  $I$  is derived from the nodal values on the normalized gradient image. Unlike the stiffness calculation in [13], which takes the average of two nodal values on a spring, we apply a weighted sum of nodal values as shown in Eq. (36). This implies that the node closer to the feature vertices will contribute more to the stiffness.

$$I = \frac{d_j}{d_i + d_j} S_i + \frac{d_i}{d_i + d_j} S_j, \quad (36)$$

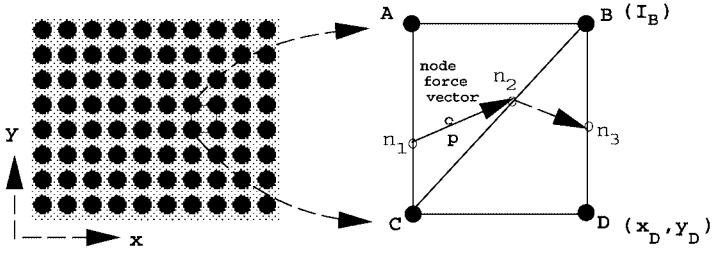


**FIG. 24.** Node displacement within a triangle area in each step:  $n_1$ : node start position;  $n_2$ : node end position;  $n_3$ : node end position in next step.

where  $S_i$  and  $S_j$  are the nodal values on the normalized gradient image at nodes  $i$  and  $j$ , respectively.  $d_i$  (or  $d_j$ ) is the minimum distance from node  $i$  (or  $j$ ) to the nearest vertex in the set of extracted feature vertices.

To obtain the nodal values ( $S_i, S_j$ ), we use the conventional finite element concept to calculate the *sub-pixel* values in between the neighboring pixels. As shown in Fig. 24, we split the pixel rectangle into two triangular elements so that sub-pixels within a certain triangle (a plane) are linearly distributed with the same property. The purpose of splitting into two triangular elements is to prevent the node movement over displace in the next fine adaptation process (e.g., jump across an edge boundary in a motion step). Let  $A$  denote a pixel at position  $(x_A, y_A)$  having value  $I_A$ . Four neighboring pixels  $A, B, C, D$  are split into two triangular elements  $\triangle ABC$  and  $\triangle BCD$ . The value of sub-pixel  $p$  within  $\triangle ABC$  can be obtained from Eq. (37) (see [9])

$$I_p = a_1 y_p + a_2 x_p + a_3, \quad (37)$$

where

$$a_1 = (x_C - x_B)I_A + (x_A - x_C)I_B + (x_B - x_A)I_C \quad (38)$$

$$a_2 = (y_B - y_C)I_A + (y_C - y_A)I_B + (y_A - y_B)I_C \quad (39)$$

$$a_3 = (x_B y_C - x_C y_B)I_A + (x_C y_A - x_A y_C)I_B + (x_A y_B - x_B y_A)I_C. \quad (40)$$

*Proof.* The linear interpolating polynomial must be of the form as in Eq. (37). At each of the node points, the following interpolation function should be satisfied:

$$I_A = a_1 y_A + a_2 x_A + a_3 \quad (41)$$

$$I_B = a_1 y_B + a_2 x_B + a_3 \quad (42)$$

$$I_C = a_1 y_C + a_2 x_C + a_3. \quad (43)$$

Solving equation group (41)–(43) for the values of  $a_1, a_2, a_3$  yields

$$a_1 = \frac{1}{2S} [(x_C - x_B)I_A + (x_A - x_C)I_B + (x_B - x_A)I_C] \quad (44)$$

$$a_2 = \frac{1}{2S} [(y_B - y_C)I_A + (y_C - y_A)I_B + (y_A - y_B)I_C] \quad (45)$$

$$a_3 = \frac{1}{2S} [(x_B y_C - x_C y_B)I_A + (x_C y_A - x_A y_C)I_B + (x_A y_B - x_B y_A)I_C], \quad (46)$$

where  $S$ , the area of the triangle, is given by the formula

$$S = \frac{1}{2}(x_B y_C - x_C y_B + x_C y_A - x_A y_C + x_A y_B - x_B y_A). \quad (47)$$

because neighboring pixels have the following relation:

$$x_A = x_C, \quad y_A = y_B, \quad y_C - y_A = 1, \quad x_B - x_A = 1. \quad (48)$$

Substituting the above expressions into Eq. (47), we obtain  $S = 0.5$ , and the scaling coefficient  $\frac{1}{2S} = 1$ . Then  $a_1$ ,  $a_2$ , and  $a_3$  are obtained using Eqs. (38)–(40).

Similar equations can be used if the point  $p$  is within  $\triangle BCD$ .

(2) Fine adaptation: After the mesh stabilizes, fine adjustments can be done by the EOM method for making meshes converge to the image “tightly.” Assuming that the image intensity changes continuously over the spatial domain, the gray values in between pixels can be obtained from Eq. (37). The criterion of the fine movement of nodes is that *only movements that decrease the node energy stored in the connected springs are allowed*. The node energy calculation and node motion rules are described below:

- Obtain node force: Of all the nodes on the mesh except the boundary vertices, find a node with the largest value of the nodal force using Eq. (34), e.g.,  $\mathbf{g}_i$ . Within a sub-pixel domain (triangle area), search sub-pixels along the direction of the  $\mathbf{g}_i$  vector in order to find one having minimum node energy.

- Obtain node energy: The strain energy  $E_{ij}$  stored in a spring  $ij$  is calculated as follows:

$$E_{ij} = C_{ij}(\|\mathbf{r}_{ij}\| - l_{ij})^2. \quad (49)$$

Node energy  $E_i$  is defined as the summation of the energy stored in all the springs connected to node  $i$ ; i.e.,

$$E_i = \sum_{j \in M_i} E_{ij}. \quad (50)$$

- Displacement of a node: Displacement of a node at a step is along the direction of the resultant nodal force. Theoretically, a node should move to a new position within the triangle domain, where the node energy is a local minimum. To simplify the computation, in the current implementation, we calculate the node energy in three positions (i.e., node start position (e.g.,  $n_1$ ), middle position (e.g.,  $p$ ), and node end position (e.g.,  $n_2$ )). The position with the minimum node energy is the new position that the node is allowed to move to. So a displacement at a step is only within a triangular area (including the boundary lines  $AC$  and  $BC$ , for example, in Fig. 24 from the node start position to the node end position). The maximum displacement of a node in one step will not exceed the distance between two adjacent pixels.

The rules for moving a node to a new position follow two conditions:

- Check the node energy at the start position and the end position. The energy must decrease; this ensures that the spring system has reached a state with less energy.

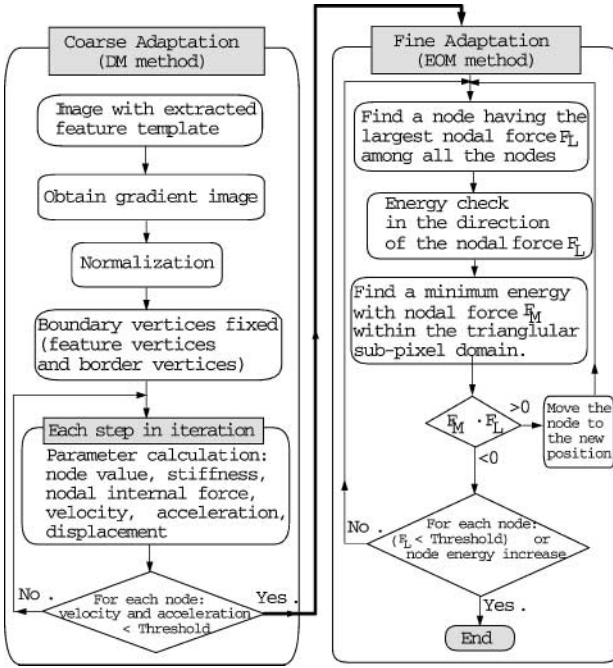


FIG. 25. Schematic diagram of the extended adaptive mesh method.

—To prevent the reversal of nodal force in the new position, the inner product of the force vector ( $F_L$ ) at the node position with the force vector ( $F_M$ ) at the new position must be greater than zero; this prevents the oscillating movement of nodes.

If the two conditions above are satisfied, the node is allowed to move to the new position. Otherwise, the node stays in its current place, and the procedure checks the node with second largest force, repeats the above procedure and continues until no node satisfies the above two conditions or the largest nodal force in the mesh is small enough (less than a certain threshold). Figure 25 shows a flow chart of the extended adaptive mesh algorithm in its current implementation.

EOM makes the mesh movement in the direction of mesh energy decrease instead of decreasing the node velocities and accelerations. The model mesh will gradually fit the image features and make the adaptation highly accurate. An example of the mesh adaptation in two steps on eye images (Fig. 9) is shown in Figs. 26 and 27. Figure 26 shows the animated

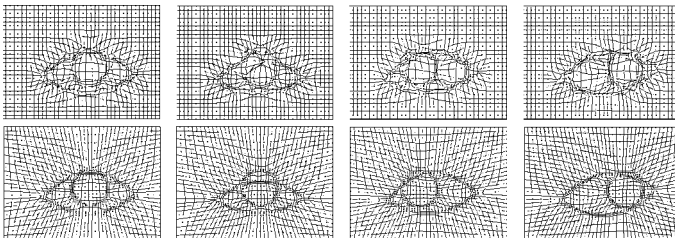
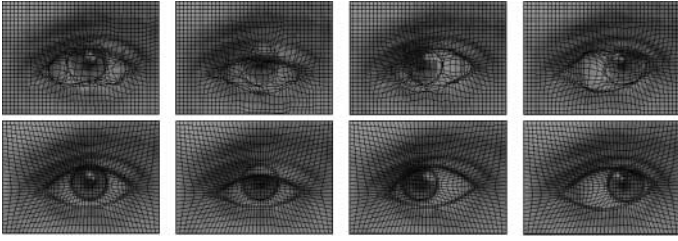


FIG. 26. Eye movement. (Top) coarse adaptation using DM method ( $m_i = 1.2$ ,  $\gamma_i = 1.2$ ,  $k_1 = 1.0$ ,  $k_2 = 9.0$ , threshold of  $v_i$  and  $a_i$  are 60.0 at the time of stopping adaptation). (Bottom) fine adaptation using EOM method (the largest nodal force is 0.05 when adaptation is stopped).



**FIG. 27.** Overlapped eye mesh: coarse adaptation (top); fine adaptation (bottom).

eye sequence after the first step (DM) and the second step (EOM), in which a plane mesh is used for testing our extended adaptive mesh algorithm. The overlapped results of coarse and fine adaptations are shown in Fig. 27. The improvement of the adaptation accuracy from coarse adaptation (DM) to fine adaptation (EOM) can be clearly seen by comparing the top sequence with the bottom sequence in Figs. 26 and 27.

Figure 28 shows some sample results of model adaptation on an expressive face. However, this procedure is time-consuming. Table 2 compares the time spent on the computation of DM and EOM when running on a SGI-O2 machine. For DM, each time step requires the evaluation of velocity and acceleration for all of the nodes; for EOM, each node requires the evaluation of internal force, nodal energy at three positions in sub-pixel domain (triangle element). In DM, all the nodes move simultaneously, while in EOM, the node movement is one by one until no nodal energy is further reduced. So EOM is more time consuming than DM (as shown in Table 1). Although the two-step adaptation method produces accurate results for model adaptation, real-time implementation is difficult because of computation time. Speeding up the process of EOM and DM is highly desired in our future work. In our current implementation, the maximum force that satisfies the displacement criteria is searched from all the nodes after each movement of a node, which takes significant computation time. One alternative is to move a node until the node cannot be moved any further, while keeping the neighboring nodes fixed. This change is expected to reduce the search time and improve the efficiency of the EOM adaptation process.

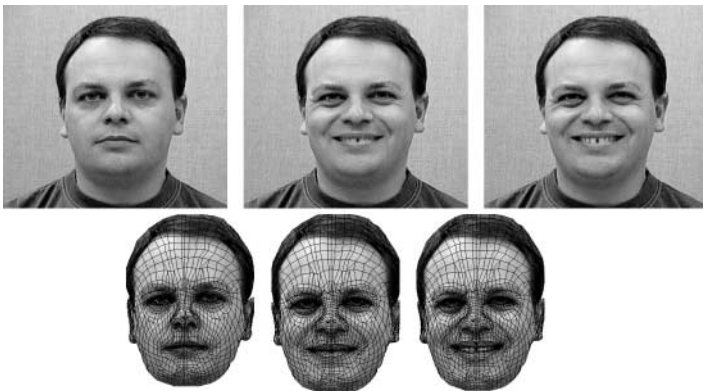


**FIG. 28.** Extended dynamic mesh adaptation. Top row: original image sequence (frame 1, 19, 21). Bottom row: adapted face model.

**TABLE 2**  
**Computation Time in DM and EOM (Note That**  
**above Numbers Represent the Average Time per**  
**Frame in the Individual Sequence)**

Experimental sequences	Computation time	
	DM (s/frame)	EOM (s/frame)
Tested eyes	6.5	9.7
Mario face	11.4	17.3

#### 4. ACTIVE TEXTURE DETECTION

After the facial model is fitted onto a face in a video sequence, the facial expressions are represented by a series of deformed facial models. As we discussed in Section 1, a deformed facial model represents only a geometric structure of a facial expression, which mainly reflects the expression of the eyes and mouth areas. This is not enough to represent a realistic vivid expression of a face. To reconstruct a lifelike expression of a face, it is necessary to provide the texture information of the face corresponding to the individual expression. The fitted model sketches the accurate location of texture areas. Since the size and shape of textures of interest vary with different expressions, the adapted facial model must be warped to a standard shape and size. Here we choose the first frame model as a standard model. We assume the first frame shows a natural expression with front view of a face, and this standard model and the corresponding texture have been stored in both sides (sender and receiver). A face model consists of a number of triangle elements. Figure 29 shows the principle of the geometric transformation with a triangle element. A pixel  $k$  within a triangle element  $P$  is transformed into a new pixel position  $k'$  within the standard triangle element  $P'$ , as formulated in Eq. (51).

$$\mathbf{k}' = \mathbf{T} \cdot \mathbf{k}, \quad (51)$$

where  $\mathbf{k} = [x_k, y_k, 1]^T$ ,  $\mathbf{k}' = [x_{k'}, y_{k'}, 1]^T$ . The transformation matrix  $T$  is derived from the relationship of the two triangle elements, as shown in Eqs. (52) and (53).

$$\mathbf{P}' = \mathbf{T} \cdot \mathbf{P} \quad (52)$$

$$\mathbf{T} = \mathbf{P}' \cdot \mathbf{P}^{-1}, \quad (53)$$

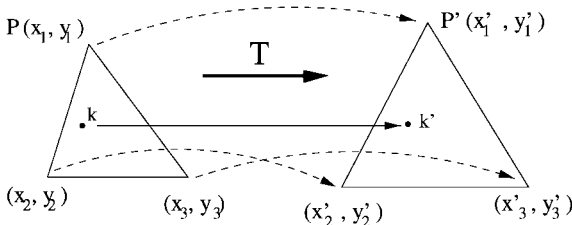


**FIG. 29.** Texture transformation within a triangle.

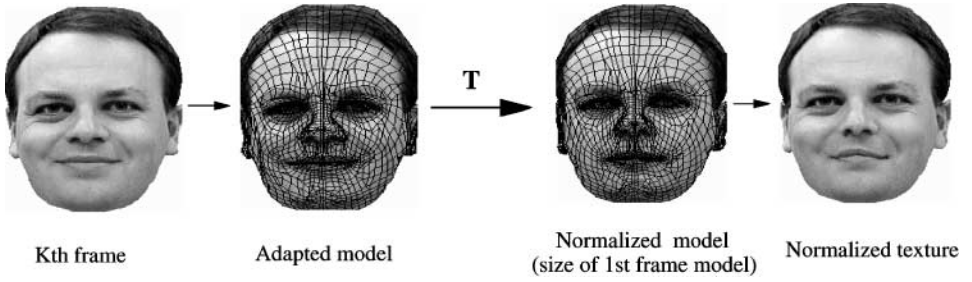


FIG. 30. Example of whole face texture transform: from 15th model (texture) to first frame model (texture).

where

$$\mathbf{P}' = \begin{bmatrix} x'_1 & x'_2 & x'_3 \\ y'_1 & y'_2 & y'_3 \\ 1 & 1 & 1 \end{bmatrix}, \quad \mathbf{T} = \begin{bmatrix} a_1 & b_1 & c_1 \\ a_2 & b_2 & c_2 \\ 0 & 0 & 1 \end{bmatrix}, \quad \mathbf{P} = \begin{bmatrix} x_1 & x_2 & x_3 \\ y_1 & y_2 & y_3 \\ 1 & 1 & 1 \end{bmatrix}. \quad (54)$$

Figure 30 shows an example of model transformation from  $k$ th ( $k = 15$ ) frame model to first frame model, and the corresponding textures. After the normalization, the subsequent faces with different expressions have the same shape, but different texture, than the first frame.

Since the fiducial points are extracted in the previous stage, the TOI areas can be determined by the geometric relationship of these fiducial points. Figure 2c shows the textures of interest formed from the fiducial point locations. For example, a forehead wrinkle area is a quadrilateral, which is limited to the leftmost and the rightmost areas of eyebrows in width, and the bottom line of hair and the top line of eyebrows in height; a glabella wrinkle area is a block in between the inner eye corners (or inner eyebrow corners, whichever has smaller distance) in width, and the top line of eyebrows and corner line of inner eyes in height; a crows-feet wrinkle occurs between the outside corner of the eyebrow and top of the nose in height, and the outside corner of the eye and the hair contour in width; a nasolabial area is a polygon which is formed by the side of the nose, outside corner of the mouth, and outside corner of the eye. To reduce the computation time, the size and shape of the extracted textures are renormalized to a standard size and shape, which is smaller than the actual size, using the geometric transformation method in Fig. 29. Figure 2d shows the normalized TOI in wrinkle and eyes and mouth areas.

Although the textures of interest are extracted in each frame, not all the textures extracted contribute to the facial expression synthesis. To represent the facial texture efficiently, only the *active textures*, which are the typical textures representing significant facial expression, need to be transmitted. The active texture detection conforms to the following criteria: If we view a specific texture of interest along consecutive frames, for example, the nasolabial wrinkle texture, each nasolabial wrinkle texture of the successive frame is correlated with the first frame to a certain degree. The higher the correlation computed between two nasolabial wrinkle textures, the closer their similarity is. In other words, the active wrinkle generated from the different expressions can be estimated by a lower correlation between the wrinkle of the current frame and the initial first frame, so do the mouth and eye areas. The correlation coefficient  $C_w(w_{t_0}, w_{t_k})$  of a certain TOI  $w$  between the  $t_k$  frame and  $t_0$  frame is

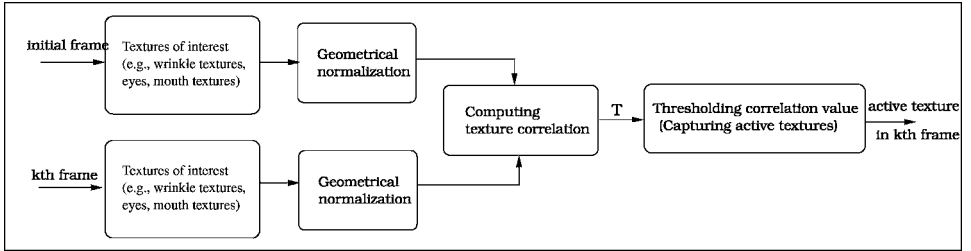


FIG. 31. Diagram of active texture (AT) detection.

computed as

$$C_w(t_0, t_k) = \frac{E_w(w_{t_0}w_{t_k}) - m_{w_{t_0}}m_{w_{t_k}}}{\sigma_w(t_0)\sigma_w(t_k)}, \quad (55)$$

where  $E_w(\cdot)$  is a mean operation,  $m_{w_{t_0}}$ ,  $\sigma_w^2(t_0)$ , and  $m_{w_{t_k}}$ ,  $\sigma_w^2(t_k)$  are the means and variances of the normalized TOI at frame  $t_0$  and frame  $t_k$ , respectively. The higher the value of  $C_w(w_{t_0}, w_{t_k})$ , the lower the probability of the region being an active area. A TOI area showing a large difference from the initial frame (i.e., low correlation value) is extracted as an active area. By doing this, a very limited number of active textures need update, reducing the amount of information that needs to be transmitted. Figure 31 shows the procedure of active texture detection.

## 5. ACTIVE TEXTURE COMPRESSION

Each active area represents a class of images on a specific region of a face. When compressing such a clearly defined class of images (e.g., active wrinkle textures, active mouth, and eyes textures), all-purpose basis functions (such as FFT, DCT, etc.) are obviously not the best choice. A set of active textures of a person is a class of textures with the same statistical property, which in general represents a statistical resemblance determined by the action of different facial expressions. For example, normally the forehead wrinkle has horizontal folds; the crows-feet wrinkle has smile-shape oblique folds; the nasolabial wrinkle has parentheses-shape folds, etc. With these specific classes of textures, transformations associated with a specific statistical property is obviously a good choice, i.e., K-L transformation (principal component analysis). The principal component analysis method provides a more efficient and adaptive form to represent active textures and therefore saves more bits while keeping the quality reasonable, as compared to DCT-based methods (such as JPEG and MPEG). By using this method, the output image can be described by the texture bases (called *eigen textures*). Since we only compute the textures of interest which have small areas, the computation load and storage capacity are greatly alleviated. This idea is similar to the strategy presented previously by Pentland *et al.* [28], Strom *et al.* [17], and Nishino *et al.* [18] in which the whole face image is divided into blocks; however, our method has an even fewer number of textures to compute.

We have defined nine active texture areas on a face. Suppose each area has  $M$  textures as an individual training set; each texture has  $N$  pixels. First, the color texture image in RGB pixels with 24-bit depth is compressed into YUV format using 4 : 1 : 1 subsampling

( $U = C_r, V = C_b$ ). Each texture  $i$  in a training set is converted to a vector  $\mathbf{x}_i$  with a dimension of  $1 \times 1.5 N$  by raster scanning the pixel values in each color band as shown in Eq. (56).

$$\mathbf{x}_i = [x_{i,1}^Y, \dots, x_{i,N}^Y, x_{i,1}^U, \dots, x_{i,N/4}^U, x_{i,1}^V, \dots, x_{i,N/4}^V]. \quad (56)$$

Then, the vectors in each training set forms an individual texture space  $\mathbf{x}$ ,

$$\mathbf{x} = [\mathbf{x}_1^T, \mathbf{x}_2^T, \dots, \mathbf{x}_M^T]^T. \quad (57)$$

The mean texture of each space is computed from their own training set—i.e.,  $\mathbf{m}_x = \mathbf{E}\{\mathbf{x}\}$ —the average of the texture vectors in texture space  $\mathbf{x}$ .  $\mathbf{C}_x$  is defined as a covariance matrix of the texture space  $\mathbf{x}$ ,

$$\mathbf{C}_x = \mathbf{E}\{(\mathbf{x} - \mathbf{m}_x)(\mathbf{x} - \mathbf{m}_x)^T\}. \quad (58)$$

The transformation from a texture space  $\mathbf{x}$  into an eigen space  $\mathbf{y}$  is represented as

$$\mathbf{y}_i = \mathbf{A}(\mathbf{x}_i - \mathbf{m}_x), \quad (59)$$

where  $\mathbf{A}$  is a matrix whose rows are formed from the eigen vectors of  $\mathbf{C}_x$ , ordered so that the first row of  $\mathbf{A}$  is the eigen vector corresponding to the largest eigen value, and the last row is the eigen vector corresponding to the smallest eigen value.

After the K-L transform is performed,  $1.5 N$  texture bases (eigen textures) are created and sorted in decreasing eigen value order. To reconstruct active textures with adequate accuracy and to efficiently compress the data,  $n$  texture bases ( $n \ll N$ ) are selected to form a transform matrix. The new texture to encode is projected onto the  $n$  texture bases. The active texture is now represented by  $n$  K-L coefficients and the corresponding set of texture bases. The  $n$  K-L coefficients can then be quantized to lower bit rates.

Because the transform matrix is derived from the statistical property of the texture, the population of the vectors in the training set directly affects the efficacy of the transformation. Increasing the size of the training set would increase the coding efficiency and the image quality [17]. Therefore, besides inputting the active textures into the training sets, we also add their mirror texture into it. For example, the left side of the nasolabial wrinkle texture would be more or less similar to the mirrored one of the right side, so the mirrored texture of the right side of the nasolabial wrinkle can be added to the training set for the left nasolabial wrinkle texture.

With the K-L transformation, the advantage of the partial texture update will be demonstrated in the section on experimental results.

## 6. FACIAL TEXTURE SYNTHESIS AND EXPRESSION GENERATION

Since the facial texture for each frame is synthesized by the first frame image (for example, showing a natural expression) and the corresponding decoded active textures, simply texture mapping is not good enough on a final appearance; especially on the boundary of the wrinkle texture, the sharp brightness transition is obviously seen. To overcome this drawback, a temporal blending method is applied to smooth the texture boundary, in which the brightness

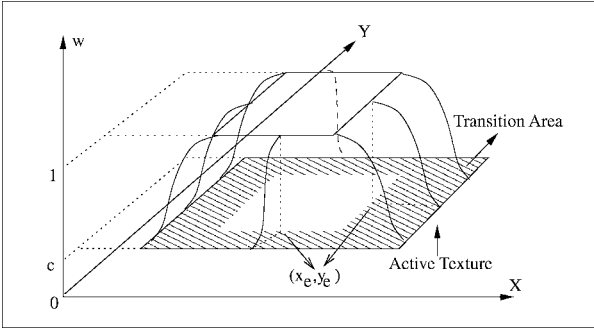


FIG. 32. The weight value selection for texture blending.

of the active texture is linearly blended with the image of the first frame on the boundary. The blending weight is in the range between 0 and 1; the value being a function of the pixel position in the active texture. In the large central area of the texture, the weight is set to 1. In the transition area the value decreases from 1 to 0, as the texture gets closer to the boundary. The blended texture value is computed as

$$b_k = (1 - w) \cdot f_1 + w \cdot f_k \tag{60}$$

$$w = \begin{cases} 1 & (x, y) \text{ within a central area or on the border;} \\ \frac{r}{\sqrt{2\pi}\sigma} e^{-\frac{(x-x_e)^2+(y-y_e)^2}{2\sigma^2}} + c & (x, y) \text{ within transition area,} \end{cases} \tag{61}$$

where  $b_k$  is the blended value of the  $k$ th frame active texture at the location  $(x, y)$ .  $f_1$  and  $f_k$  are the active texture values in frames 1 and  $k$ , respectively.  $w$  is the blending weight

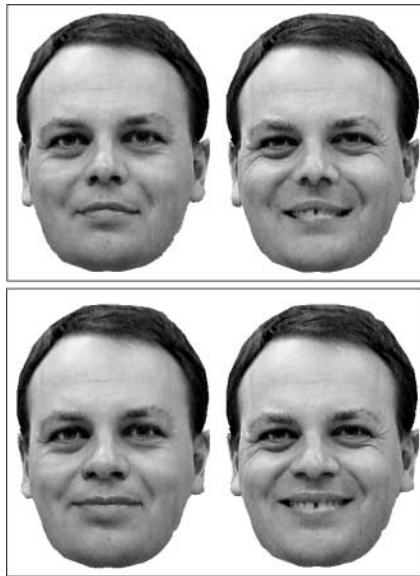


FIG. 33. Expression synthesis using partial texture update and blending technique. Top two: synthesized 2D facial texture using the 1st frame texture and the active textures of frame 15 and frame 19, respectively. Bottom two: Using the left synthesized textures to map (warping) onto the 3D face model of frame 15 and frame 19. This is a reverse normalization procedure (de-normalization) of Fig. 30.

as depicted in Fig. 32.  $(x_e, y_e)$  is a variable position on the edge (borderline between the central area and the transition area).  $r$  is a factor for normalizing the values; here  $r$  is set to  $\sqrt{2\pi}\sigma$ . The response of the human visual system tends to “overshoot” around the boundary of regions of different intensity. The result of this brightness perception is to make areas of constant intensity appear as if they had varying brightness. This is a well-known *Mach-band effect*. To alleviate the Mach-band effect, in the transition area the weight value is determined by the Gaussian distribution centered at variable positions of  $(x_e, y_e)$  to make texture fusion smoother and the intensity difference around the boundary region smaller. The variance  $\sigma$  and constant  $c$  are adjustable, which are set here as  $\sigma = 1.0$ ,  $c = 0.2$ . This blending process makes the two textures be synthesized visually smoother from our experiment. Figure 33 shows the example results of 2D texture synthesis in the normalized size, and its mapping on the 15th frame model and 19th frame model using the inverse normalization process.

## 7. EXPERIMENTAL RESULTS

A video sequence showing the different expressions of a person is the input for our experiment. The resolution of each frame is  $550 \times 700$  pixels. Figure 34 (row 1) shows the results of model adaptation using the extended dynamic mesh matching algorithm. Row 2 shows the original face textures. The results of face image normalization, and extracted textures of interest (e.g., wrinkle, eye, and mouth) are shown as polygons in row 3. Row 4 shows the group of textures of interest, which are geometrically normalized into the size of  $50 \times 90$  for forehead texture,  $30 \times 30$  for glabella texture,  $40 \times 40$  for both left and right crows-foot textures,  $80 \times 40$  for both left and right nasolabial textures,  $50 \times 80$  for mouth texture, and  $40 \times 80$  for both left and right eye textures.

To detect the active texture among the TOI, the correlation values of the TOI between the first frame and the subsequent frames are computed. The temporal correlation of six wrinkle textures and eye–mouth textures are changed along with different expressions, the textures whose correlation values are below the threshold line are detected as active textures. The threshold is selected by a statistical result. We use five sets of video sequences with five people’s expressions as a training set. Each video sequence has 65 frames, which shows the individual’s smiling, laughing, sad, worry, and surprise (the first frame shows a natural expression). The textures of interest in different areas are extracted individually. Then the correlation of the first frame texture and the subsequent frame texture is calculated. For each sequence, we obtained a threshold by observing the apparent change in the expressions. Then, the final threshold is obtained by the average of the five thresholds corresponding to the five persons’ textures. The threshold selection is done by the above training process. With more training samples, the accuracy of the threshold increases. The threshold value obtained is 0.8 (forehead), 0.85 (glabella), 0.7 (crowsfoot), 0.5 (nasolabial), 0.45 (mouth), and 0.35 (eye). Figures 35 and 36 show the example of active texture detection, in which an original video showing a person’s different expressions is input to our system. The person’s expression changes in several stages, i.e., *natural*  $\rightarrow$  *eye-closing*  $\rightarrow$  *smiling*  $\rightarrow$  *laughing*  $\rightarrow$  *back-to-natural*  $\rightarrow$  *worrying or sad*  $\rightarrow$  *surprise*. In the Chart I, the active texture of the forehead wrinkle is captured when the expression goes to “surprise,” where the forehead horizontal-shape wrinkle is formed. In Chart II, the active glabella texture (in between the eyebrows) is detected when the “worry or sad” expression is enacted. In Charts III and IV, the curves of texture correlation in crowsfoot area (outer corners of eyes) and the nasolabial

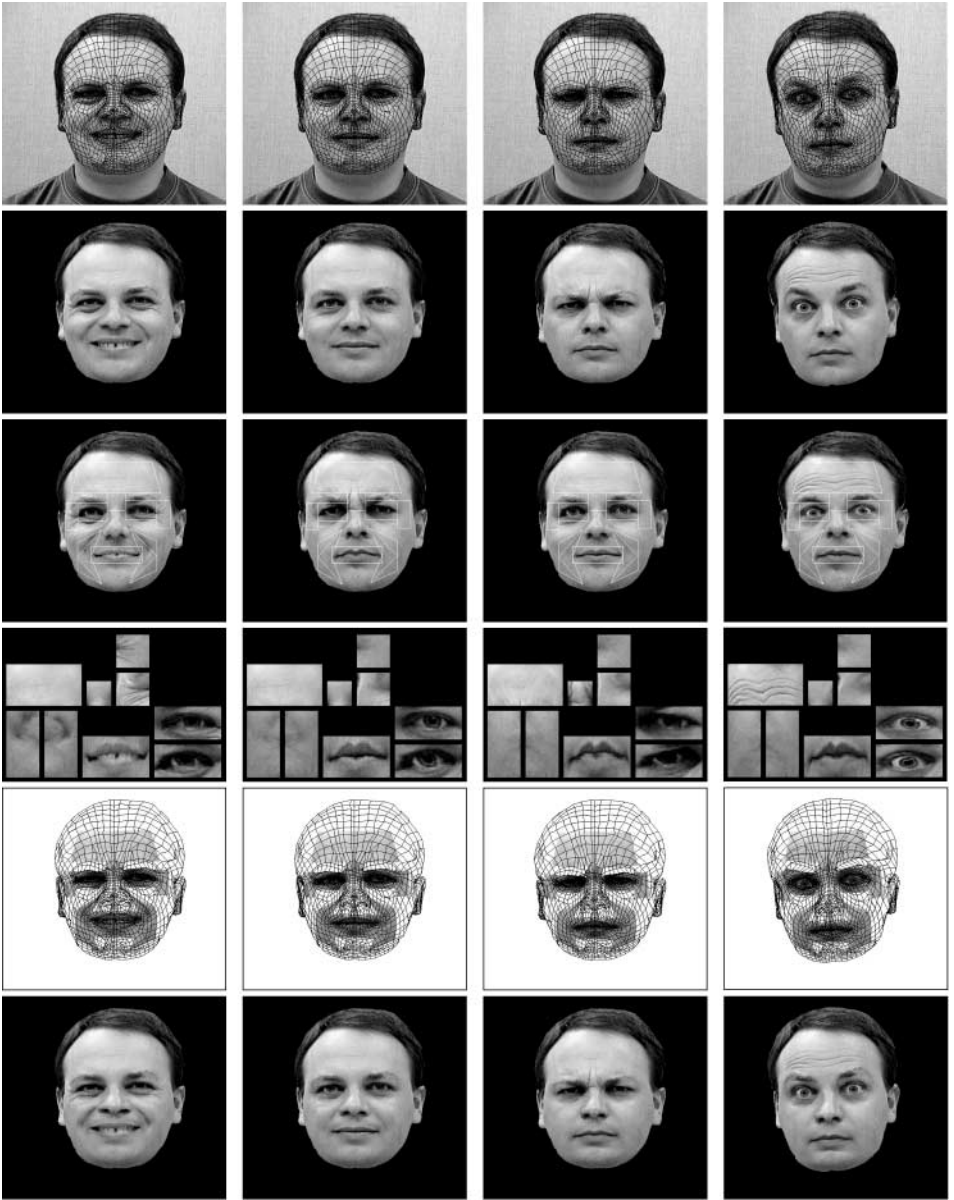


**FIG. 34.** Facial texture synthesis: Row 1: fitted model. Row 2: original texture. Row 3: normalized face texture. Row 4: normalized textures of interest. Row 5: updated textures of interest. Row 6: synthesized face (from left to right: frame 20, 32, 42, 62 of video Mario).

regions go down to the threshold value for the “smiling” and “laughing” expressions, the eye-corner wrinkles with smile-shape oblique folds and mouth–nose side wrinkles with parentheses-shape folds are generated. Chart V indicates the active mouth textures detected when the mouth is opening to expose the teeth. Active eye textures are estimated by the correlation values lower than the threshold in Chart-VI, there are three locations showing the obvious change with eye textures, which are in the stages of “eye closing,” “sad” and “surprise.”

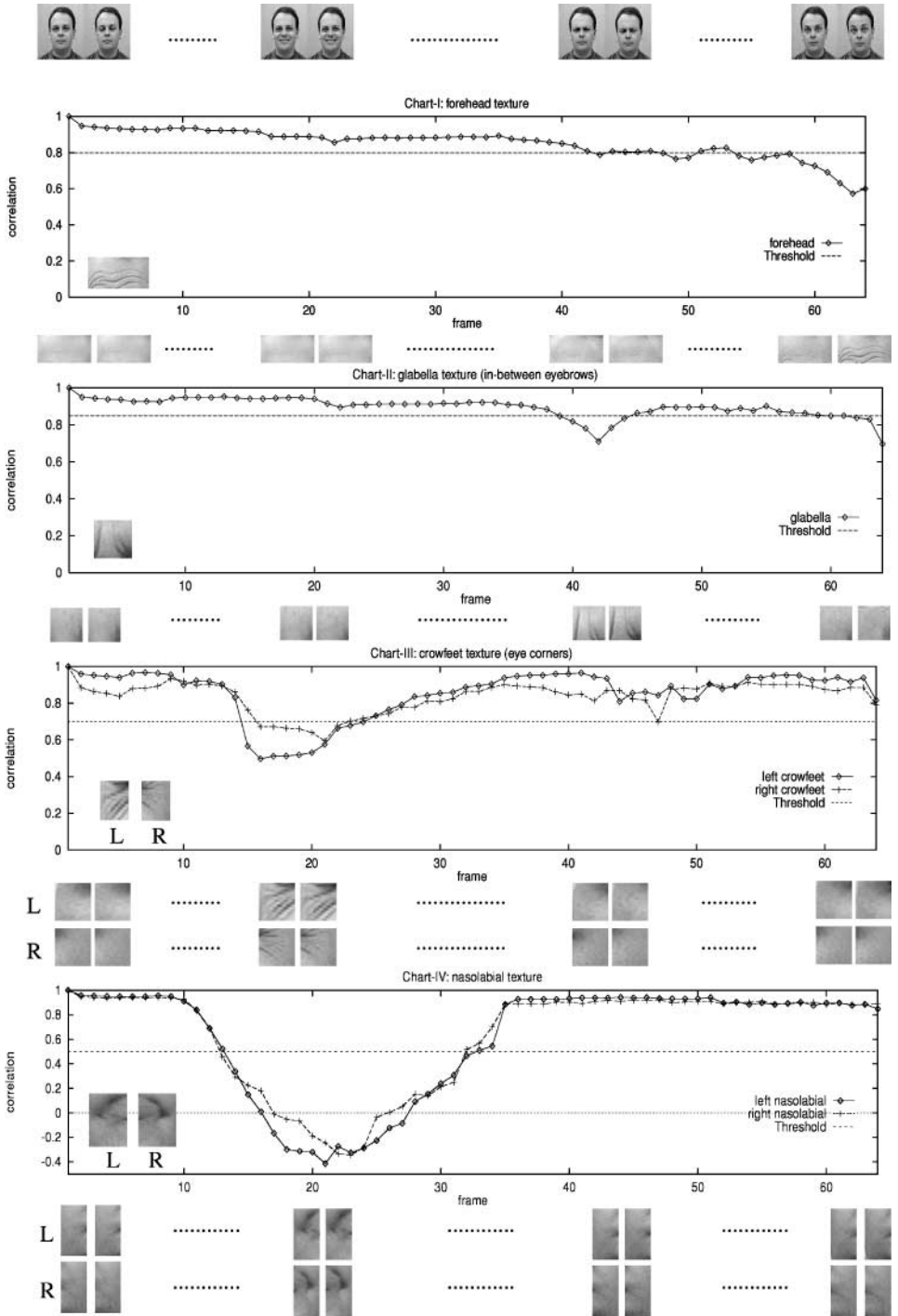


**FIG. 35.** Chart of temporal correlation of wrinkle textures between the first frame (left-most face of the top row) and the subsequent frames. The top is an original video sequence showing a person's face with different expressions from left to right, such as initial natural expression, eyes closing, smiling, laughing, worry and sad, and surprise.

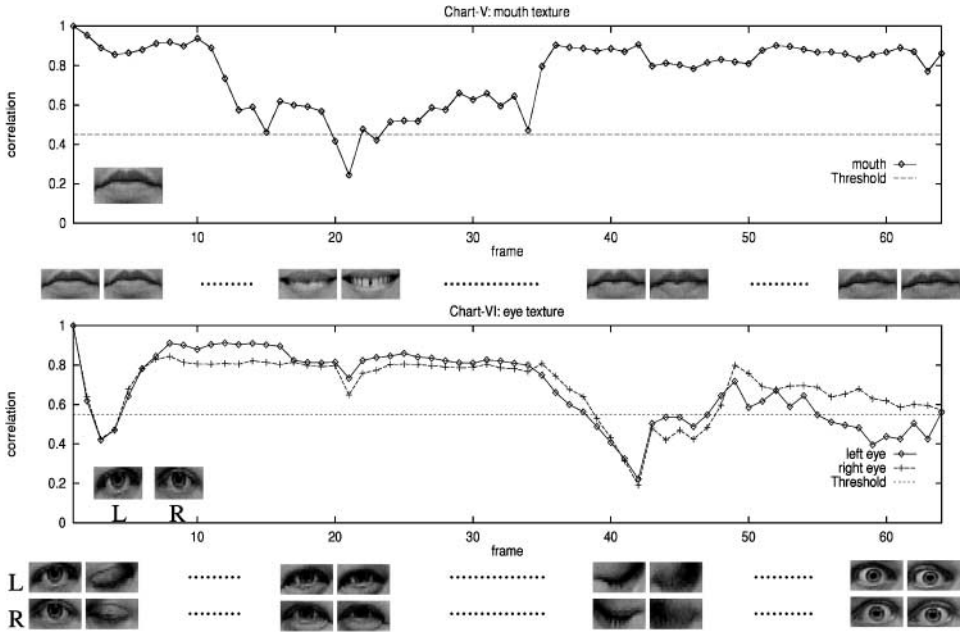


**FIG. 36.** Chart of temporal correlation of mouth and eyes textures between the first frame and the subsequent frames. The input video shows a person's face acting different expressions from left to right, such as initial natural expression, eyes closing, smiling, laughing, worry and sad, and surprise.

The low temporal correlation value distinguishes the active texture among the textures of interest. For example, the wrinkle corresponding to a lower value shows an obviously different wrinkle shape than the others. Hence, the correlation method has a good performance in detecting the active texture in an expressive face.

After the active textures on an individual face are obtained, the principal component transformation is applied to map the active textures into the eigen space. In our experiment, each active area has 200 textures as training vectors. Because we take into account only nine active areas and each one has a small dimension, a small number of eigen textures is sufficient to describe the principal characteristics of each active texture and is enough to reconstruct the active texture with an adequate fidelity; i.e., 25 eigen textures (texture bases) are selected for each of forehead texture, nasolabial texture (both left side and right side), mouth texture, and eye texture (left side and right side); and 12 eigen textures are selected for each of crowsfeet texture (left and right) and glabella texture. Thus, if all nine TOI are detected to be active textures in a frame ( $550 \times 700$  pixels), at most  $186 (=25 \times 6 + 12 \times 3)$  data points need to be transmitted, each data point can be quantized with 5 bits, to produce

**TABLE 3**

**Comparison of the Partial Texture Update and Whole Texture Update**

Property	Partial texture	Whole texture
Quality	34.6 dB	35.5 dB
Subjective	4/5 (good)	Not available
Compression	<40 kbits/s	>200 kbits/s
Computation	Dimension (<50*90)	<600*600

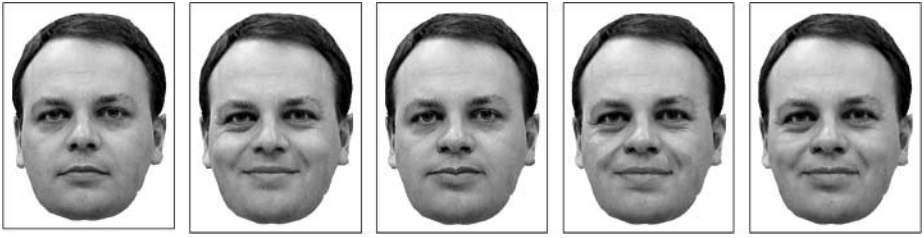


**FIG. 37.** (1) Original first frame. (2) Original 15th frame. (3) Synthesized face (15th frame) without wrinkle texture update (only first frame texture used). (4) Synthesized face with wrinkle texture update but no blending the edges. (5) Synthesized face (frame 15) with texture update and texture blending.

data for each frame totalling 116 bytes to achieve a SNR of 34.6 dB. Considering a frame rate of 30 Hz, the bit rate for texture update is about 27 kbit/s at the maximum. In an actual situation, the texture update does not occur in every TOI, neither on every frame. Therefore, the bit cost is much less than the above maximum estimation. If the animation parameters and geometric information are counted, the transmission rate will increase no more than 10 kbit/s if using the PCA + DCT compression approach [34]. So the total bit cost would be less than 40 kbit/s. Compared to the full face texture update approach [17] (where the data encoded for each frame is about 1632 bytes in the case of  $600 \times 600$  pixels textures quantized with 5 bits per coefficient for yielding a SNR of 35.5 dB; the bit rate is over 200 kbit/s with 25 frame/s rate), the computation cost is greatly reduced and the coding efficiency is obviously improved to a large degree using our active texture update method. The comparison of the coding efficiency, the computation load, and the quality evaluation are illustrated in Table 3. To synthesize a realistic facial expression, the decoded textures are repaired in the transition border area using a temporal blending technique, and finally the textures are mapped onto the individual models in the subsequent frames, as shown in Fig. 34 (row 6). In comparison with the original video sequence, the recovered images have high visual fidelity, and the SNR is over 34 dB as measured by the ratio of the mean pixel value over the mean error value. It is obvious that the synthesis result with texture updating and blending is much better than that without texture updating and blending (as seen in Fig. 37 and Table 4 for comparison). Notice in this figure that the third face from the left, the one without texture update, does not seem to capture the smiling expression as accurately as the rightmost one, the one with texture update and blending. Also, patches around the cheeks are evident in the fourth face from the left, the one without blending.

More experiments are performed on a variety of videos showing different persons' expressions. Figures 38–41 are some sample results of video “Dima,” “Alau,” “Dana,” and

**TABLE 4**  
**Comparison of with-or-without Texture Update and Blending**

Scheme (partial texture)	Subjective (Rating)	Objective SNR (dB)
No update	2/5 (poor)	25.7 (average)
Update/no blending	3/5 (fair)	33.1 (average)
Update + blending	4/5 (good)	34.6 (average)



**FIG. 38.** Dima: (Top from left) (1) Model fitted on the head of the initial frame. (2) Original facial textures of the initial frame. (3) Texture of interests (TOI) on the initial frame. (Bottom from left) (1) Model fitted on the head of the ninth frame. (2) Original facial textures of the ninth frame. (3) Normalized texture and TOI on the ninth frame. (4) Synthesized face expression of the ninth frame. (Please compare the bottom (2) and (4).)

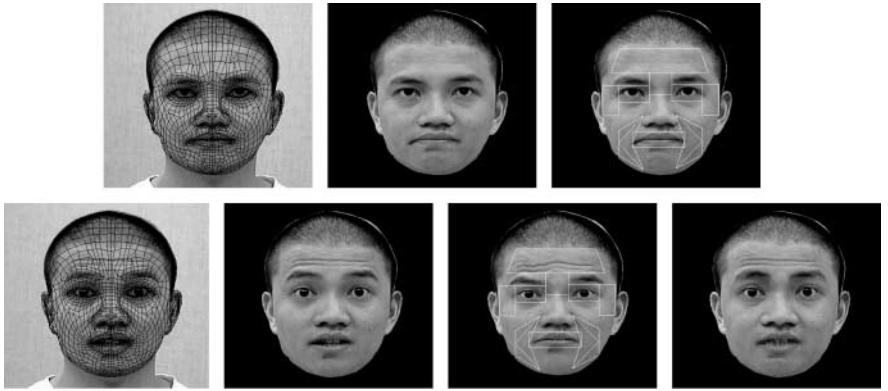


**FIG. 39.** Alau: (Top from left) (1) Model fitted on the head of the initial frame. (2) Original facial textures of the initial frame. (3) Texture of interests (TOI) on the initial frame. (Bottom from left) (1) Model fitted on the head of the 21st frame. (2) Original facial textures of the 21st frame. (3) Normalized texture and TOI on the 21st frame. (4) Synthesized face expression of the 21st frame. (Please compare the bottom (2) and (4).)

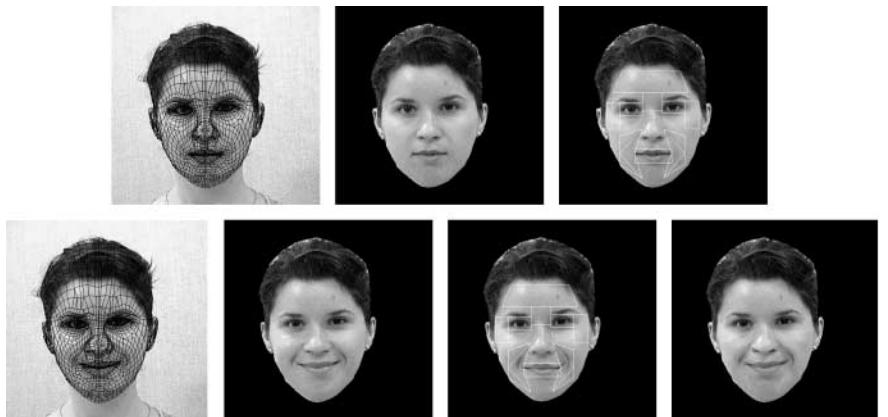


**FIG. 40.** Dana: (Top from left) (1) Model fitted on the head of the initial frame. (2) Original facial textures of the initial frame. (3) Texture of interests (TOI) on the initial frame. (Bottom from left) (1) Model fitted on the head of the 14th frame. (2) Original facial textures of the 14th frame. (3) Normalized texture and TOI on the 14th frame. (4) Synthesized face expression of the 14th frame. (Please compare the bottom (2) and (4).)

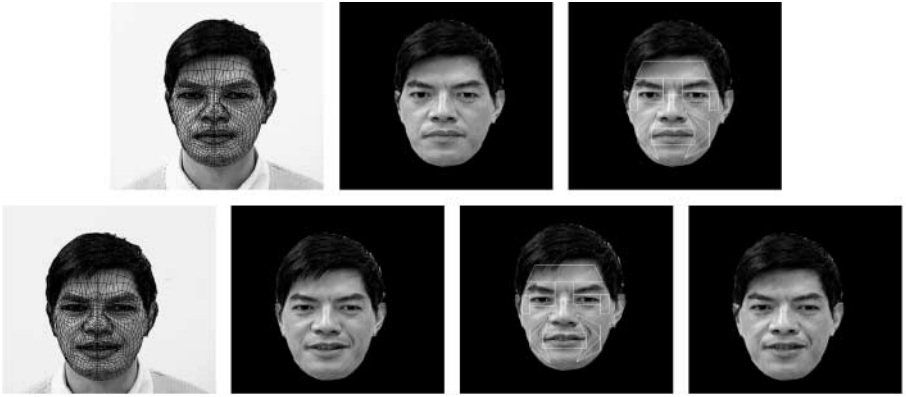


**FIG. 41.** Guan: (Top from left) (1) Model fitted on the head of the initial frame. (2) Original facial textures of the initial frame. (3) Texture of interests (TOI) on the initial frame. (Bottom from left) (1) Model fitted on the head of the 11th frame. (2) Original facial textures of the 11th frame. (3) Normalized texture and TOI on the 11th frame. (4) Synthesized face expression of the 11th frame. (Please compare the bottom (2) and (4).)

“Guan.” In general, the system performs well comparing the synthesized expressions to the original expressions perceptually. Note that the result of expression generation depends on the correctness and robustness of fiducial points detection. In the case of: (1) the initial template localization is not accurate enough, (2) the hue and saturation signals are not strong enough under certain imaging conditions, or (3) the size of feature area appears small if the image resolution is low and cannot provide enough feature information for the template matching, the system will fail to detect the correct fiducial points and will result in an incorrect texture update. We take the following strategy to deal with inaccurate fiducial point detection: comparing the results of fiducial points detected between the current frame and the previous frame; if the difference is larger than 15 pixels for any fiducial point, the result of the current frame will be discarded; instead the result of the previous frame will be borrowed for use in the current frame.

## 8. CONCLUSIONS AND FUTURE WORK

In this paper we proposed a face texture update and compression strategy for model-based coding. The experimental results show that this strategy, using the partial wrinkle texture update method, has certain advantages over the entire texture update method; more specifically, the number of coefficients that need to be transmitted is reduced significantly from the original 1632 bytes per frame to the present 116 bytes per frame. Perceptually, the high fidelity of the image quality is sustained. Notice that the temporal correlation method to detect the active texture can be potentially used for facial expression recognition. We believe that the different composition of active textures in the temporal domain has a certain relationship with the different expression representation. The investigation of this relationship would be a promising way for facial expression recognition, although this is not the purpose of the work presented in this paper. In the future, a variable resolution model update strategy will be investigated to further improve the texture mapping results. The wrinkle texture area formulation procedure and the active wrinkle estimation method also need to be improved in the areas of accuracy and robustness. In a real application, the computation load needs to be further reduced so that the system can be implemented in real time.

Note that our method can deal with scaling (i.e., head moving toward or away from the camera). However, we have not dealt with large rigid motion (large rotation) of the head during expression analysis and synthesis. We have constrained our study to a talking face with front view in the video sequence. Only minimal motion is allowed (two eyes are always visible). This strict assumption is not the case desired for a spontaneous and dynamic setting and is not expected in a real conversation. Therefore, it is necessary to address the issue of extracting *large and free* global motion of the head. An interesting future extension would be the addition of either a feature-based or a template-based method to extract such global motions. Another way of resolving this problem is to use the simultaneous estimation of global rigid motion and local non-rigid motion using an affine model of motion and spatial-temporal constraints. Note that in the case of large motion and variable lighting conditions smoothing the textures in the time direction needs to be further considered so that the continuity of the motion can be maintained.

To deal with the case of various head poses, a multiple-view texture synthesis technique needs to be investigated in our future work.

## REFERENCES

1. G. A. Abrantes and F. Pereira, An MPEG-4 SNHC compatible implementation of a 3D facial animation system, in *IWSNHC3DI'97, Rhodes, Greece, September 1997*, pp. 12–15.
2. K. Aizawa, C. S. Choi, H. Harashima, and T. S. Huang, Human facial motion analysis and synthesis with application to model-based coding, in *Motion Analysis and Image Sequence Processing* (M. I. Sezan and R. L. Lagendijk, Eds.), Kluwer Academic, Norwell, MA, 1993.
3. G. Bernd, P. Eisert, M. Magnor, E. Steinbach, and T. Wiegand, 3D imaging and compression—synthetic, hybrid or natural fit? in *International Workshop on Synthetic-Natural Hybrid Coding and Three Dimensional Imaging (IWSNHC3DI'99), Santorini, Greece, September 1999* (M. S. Strintzis et al., Eds.).
4. S. Bernoegger, Lijun Yin, A. Basu, and A. Pinz, Eye tracking and animation for MPEG4 coding, in *ICPR'98: Proceedings 14th IAPR International Conference on Pattern Recognition, Australia, August 1998*.
5. R. Brunelli and T. Poggio, Face recognition: Features versus templates, *IEEE Trans. PAMI* **15**(10), 1993, 1042–1052.
6. C. Choi, K. Aizawa, H. Harashima, and T. Takebe, Analysis and synthesis of facial image sequences in model-based image coding, *IEEE Trans. CAS Video Tech.* **4**(3), 1994, 257–275.
7. G. Chow and X. Li, Towards a system for automatic facial feature detection, *Pattern Recognition* **26**(12), 1993, 1739–1755.
8. E. R. Davies, A modified hough scheme for general circle location, *Pattern Recognition* **7**, 1988, 37–43.
9. D. J. Dawe, *Matrix and Finite Element Displacement Analysis of Structures*, Clarendon, Oxford, 1984.
10. P. Ekman and W. Friesen, *Facial Action Coding System*, Consulting Psychologists, New York, 1977.
11. P. Ellis, Recognizing faces, *British J. Psychol.* **66**(4), 1975, 409–426.
12. B. Guenter, C. Grimm, D. Wood, H. Malvar, and F. Pighin, Making faces, in *SIGGRAPH'98, Orlando, 1998*, pp. 55–66.
13. D. Terzopoulos and M. Vasilescu, Sampling and reconstruction with adaptive meshes, in *CVPR'91, 1991*, pp. 70–75.
14. F. Pighin, J. Hecker, D. Linchinski, R. Szeliski, and D. Salesin, Synthesizing realistic facial expressions from photographs, in *SIGGRAPH'98, Orlando, 1998*, pp. 75–84.
15. H. H. Chen, T. Ebrahimi, G. Rajan, C. Horne, P. K. Doenges, and L. Chiariglione, Special issue on synthetic/natural hybrid video coding, *IEEE Trans. CAS Video Tech.* **9**(2), 1999, 205–206.
16. I. Essa and A. Pentland, Coding, analysis, interpretation, and recognition of facial expressions, *IEEE Trans. PAMI* **19**(7), 1997, 757–763.

17. J. Strom, F. Davoine, J. Ahlberg, H. Li, and R. Forchheimer, Very low bit rate facial texture coding, in *IWSNHC3DI'97, Rhodes, Greece, 1997*, pp. 237–240.
18. K. Nishino, Y. Sato, and K. Ikeuchi, Eigen-texture method: Appearance compression based on 3D model, in *CVPR'99, Fort Lollins, CO*, pp. 618–624.
19. B. Haskell, P. Howarda, Y. LeCun, A. Puri, J. Ostermann, M. Civanlar, L. Rabiner, L. Bottou, and P. Haffner, Image and video coding—Emerging standards and beyond, *IEEE Trans. CAS Video Tech.* **8**(7), 1998, 814–837.
20. W. Huang and D. Goldgof, Adaptive-size meshes for rigid and non-rigid shape analysis and synthesis, *IEEE Trans. PAMI* **15**(6), 1993, 611–616.
21. P. Kierkegaard, A method for detection of circular arcs based on the hough transform, *Machine Vision Appl.* **5**, 1992, 249–263.
22. R. Koenen, F. Pereira, and L. Chiariglione, MPEG-4: Context and objectives, *Signal Process. Image Commun.* **9**(4), 1997, 295–304.
23. Y. Kunita, M. Inami, T. Maeda, and S. Tachi, Real-time rendering system of moving objects, in *Proceedings of IEEE Computer Society Workshop on Multi-View Modeling and Analysis of Visual Scenes, Fort Lollins, Colorado, June 1999*, pp. 81–88.
24. H. Li, A. Lundmark, and R. Forchheimer, Image sequence coding at very low bitrates: A review, *IEEE Trans. Image Process.* **3**(5), 1994, 589–609.
25. C. Lin and J. Wu, Automatic facial feature extraction by genetic algorithm, *IEEE Trans. Image Process.* **8**(6), 1999, 834–845.
26. M. Nahas, H. Huitric, M. Rioux, and J. Domey, Facial image synthesis using skin texture recording, *The Visual Comput. Internat. J. Comput. Graph.* **6**, 1990, 337–343.
27. F. Parke and K. Waters, *Computer Facial Animation*, A. K. Peters, Wellesley, MA, 1996.
28. A. Pentland, B. Moghaddam, and T. Starner, View-based and modular eigenspaces for face recognition, in *Proceedings of IEEE Computer Society Conference on Computer Vision and Pattern Recognition, June 1994*.
29. W. Press, S. Teukolsky, W. Vetterling, and B. Flannery, *Numerical Recipes in C: The Art of Scientific Computing*, Cambridge Univ. Press, Cambridge, UK, 1988.
30. M. Reinders, P. Beek, B. Sankur, and J. Lubbe, Facial feature localization and adaptation of a generic face model for model-based coding, *Signal Process. Image Commun.* **7**, 1995, 57–74.
31. MPEG Requirements, Overview of MPEG-4 profiles and levels, in *ISO/JTC1/SC29/WG11 N2325, Dublin MPEG Meeting, July 1998*.
32. MPEG Video and SNHC, Text of ISO/IEC FDIS 14496-2: Visual, Doc. ISO/IEC JTC1/SC29/WG11 MPEG N2501, in *Proc. Atlantic City MPEG Meeting, October 1998*.
33. MPEG Systems, Text of ISO/IEC FDIS 14496-1: Systems, Doc. ISO/IEC JTC1/SC29/WG11 MPEG N2501, in *Proc. Atlantic City MPEG Meeting, October 1998*.
34. H. Tao, H. Chen, W. Wu, and T. Huang, Compression of MPEG4 facial animation parameters for transmission of talking heads, *IEEE Trans. CAS Video Tech.* **9**(2), 1999, 264–276.
35. H. Tao and T. Huang, Explanation-based facial motion tracking using a piecewise bézier volume deformation model, in *CVPR'99, Fort Lollins, Colorado, June 1999*, pp. 611–617.
36. D. Terzopoulos and K. Waters, Analysis and synthesis of facial image sequences using physical and anatomical models, *IEEE Trans. PAMI* **15**(6), 1993, 569–579.
37. L. Yin and A. Basu, Facial feature extraction for synthesizing realistic facial expressions with wrinkles, Technique Report, CS, Univ. of Alberta, 1999, available at <ftp://ftp.cs.ualberta.ca/pub/lijun/TechReport99-facefeature.ps.gz>.
38. Lijun Yin and Anup Basu, Face model adaptation with active tracking, in *Proceedings of IEEE International Conference on Image Processing, Kobe, Japan, October 1999*.
39. A. L. Yuille, P. W. Hallinan, and D. S. Cohen, Feature extraction from faces using deformable templates, *Internat. J. Comput. Vision* **8**(2), 1992, 99–111.
40. Liang Zhang, Estimation of eye, eyebrow and nose features in videophone sequences, in *International Workshop on Coding Techniques for Very Low Bit-Rate Video (VLBV'98), Urbana, 1998*.
41. Y. Q. Zhang, F. Pereira, T. Sikora, and C. Reader, Special issue on MPEG-4, *IEEE Trans. CAS Video Tech.* **7**, 1997.